

Preferential occurrence of fast radio bursts in massive star-forming galaxies

<https://doi.org/10.1038/s41586-024-08074-9>

Received: 5 May 2024

Accepted: 18 September 2024

Published online: 6 November 2024

 Check for updates

Kritti Sharma¹✉, Vikram Ravi^{1,2}, Liam Connor¹, Casey Law^{1,2}, Stella Koch Ocker^{1,3}, Myles Sherman¹, Nikita Kosogorov¹, Jakob Faber¹, Gregg Hallinan^{1,2}, Charlie Harnach^{1,2}, Greg Hellbourg^{1,2}, Rick Hobbs^{1,2}, David Hodge^{1,2}, Mark Hodges^{1,2}, James Lamb^{1,2}, Paul Rasmussen^{1,2}, Jean Somalwar¹, Sander Weinreb¹, David Woody^{1,2}, Joel Leja^{4,5,6}, Shreya Anand¹, Kaustav Kashyap Das¹, Yu-Jing Qin¹, Sam Rose¹, Dillon Z. Dong^{1,7}, Jessie Miller¹ & Yuhan Yao^{1,8}

Fast radio bursts (FRBs) are millisecond-duration events detected from beyond the Milky Way. FRB emission characteristics favour highly magnetized neutron stars, or magnetars, as the sources¹, as evidenced by FRB-like bursts from a galactic magnetar^{2,3}, and the star-forming nature of FRB host galaxies^{4,5}. However, the processes that produce FRB sources remain unknown⁶. Although galactic magnetars are often linked to core-collapse supernovae (CCSNe)⁷, it is uncertain what determines which supernovae result in magnetars. The galactic environments of FRB sources can be used to investigate their progenitors. Here, we present the stellar population properties of 30 FRB host galaxies discovered by the Deep Synoptic Array (DSA-110). Our analysis shows a marked deficit of low-mass FRB hosts compared with the occurrence of star formation in the Universe, implying that FRBs are a biased tracer of star formation, preferentially selecting massive star-forming galaxies. This bias may be driven by galaxy metallicity, which is positively correlated with stellar mass⁸. Metal-rich environments may favour the formation of magnetar progenitors through stellar mergers^{9,10}, as higher-metallicity stars are less compact and more likely to fill their Roche lobes, leading to unstable mass transfer. Although massive stars do not have convective interiors to generate strong magnetic fields by dynamo¹¹, merger remnants are thought to have the requisite internal magnetic-field strengths to result in magnetars^{11,12}. The preferential occurrence of FRBs in massive star-forming galaxies suggests that a core-collapse supernova of merger remnants preferentially forms magnetars.

The DSA-110, situated at the Owens Valley Radio Observatory (OVRO) near Bishop, California, is a radio interferometer built for simultaneous FRB discovery and arcsecond-scale localization. The DSA-110 underwent science commissioning and performed observations between February 2022 and March 2024 with a coherent core of 48 4.65-m antennas used for FRB searching combined with 15 outrigger antennas (maximum baseline of 2.5 km) used for localization. Each antenna is equipped with a dual-polarization ambient-temperature 1.28–1.53-GHz receiver. A custom low-noise amplifier design delivering 7 K noise temperature¹³ was central to achieving sensitivity to 1.9 Jy ms FRBs (for millisecond-duration events). A real-time search for FRBs with 0.262-ms sampling and a dispersion measure (DM) range up to 1,500 pc cm⁻³ was conducted. Localization accuracies of better than ±2 arcsec (90% confidence) were achieved by comparison with coeval observations of standard astrometric reference sources (see Methods and Supplementary

Figs. 1 and 2). During these observations, 60 FRBs were successfully localized.

In this work, we limit our analysis to FRBs discovered up to November 2023 that have redshifts for all hosts detectable down to $r = 23.5$ mag, to ensure a uniform sample selection. The follow-up of a subset of FRBs discovered post-November 2023 is presented in our companion paper¹⁴. Among the 42 FRBs localized by the DSA-110 up to November 2023, 30 had a potential host-galaxy candidate in the vicinity of the FRB localization (within 10''), detectable at ≤ 23.5 mag in archival r-band data from PanSTARRS1 (PS1)¹⁵ or the Beijing-Arizona Sky Survey (BASS) from the Dark Energy Survey¹⁶. We complement these archival data with deeper ground-based optical or near-infrared (NIR) imaging observations with the Wafer-Scale Imager for Prime focus (WaSP)¹⁷ and the Wide Field Infrared Camera (WIRC)¹⁸ instruments, mounted on the 200-inch Hale Telescope at the Palomar Observatory in our follow-up campaigns (see Methods).

¹Cahill Center for Astronomy and Astrophysics, California Institute of Technology, Pasadena, CA, USA. ²Owens Valley Radio Observatory, California Institute of Technology, Big Pine, CA, USA.

³The Observatories of the Carnegie Institution for Science, Pasadena, CA, USA. ⁴Department of Astronomy and Astrophysics, The Pennsylvania State University, University Park, PA, USA.

⁵Institute for Computational and Data Sciences, The Pennsylvania State University, University Park, PA, USA. ⁶Institute for Gravitation and the Cosmos, The Pennsylvania State University, University Park, PA, USA. ⁷National Radio Astronomy Observatory, Socorro, NM, USA. ⁸Department of Astronomy, University of California, Berkeley, CA, USA. ✉e-mail: kritti@caltech.edu

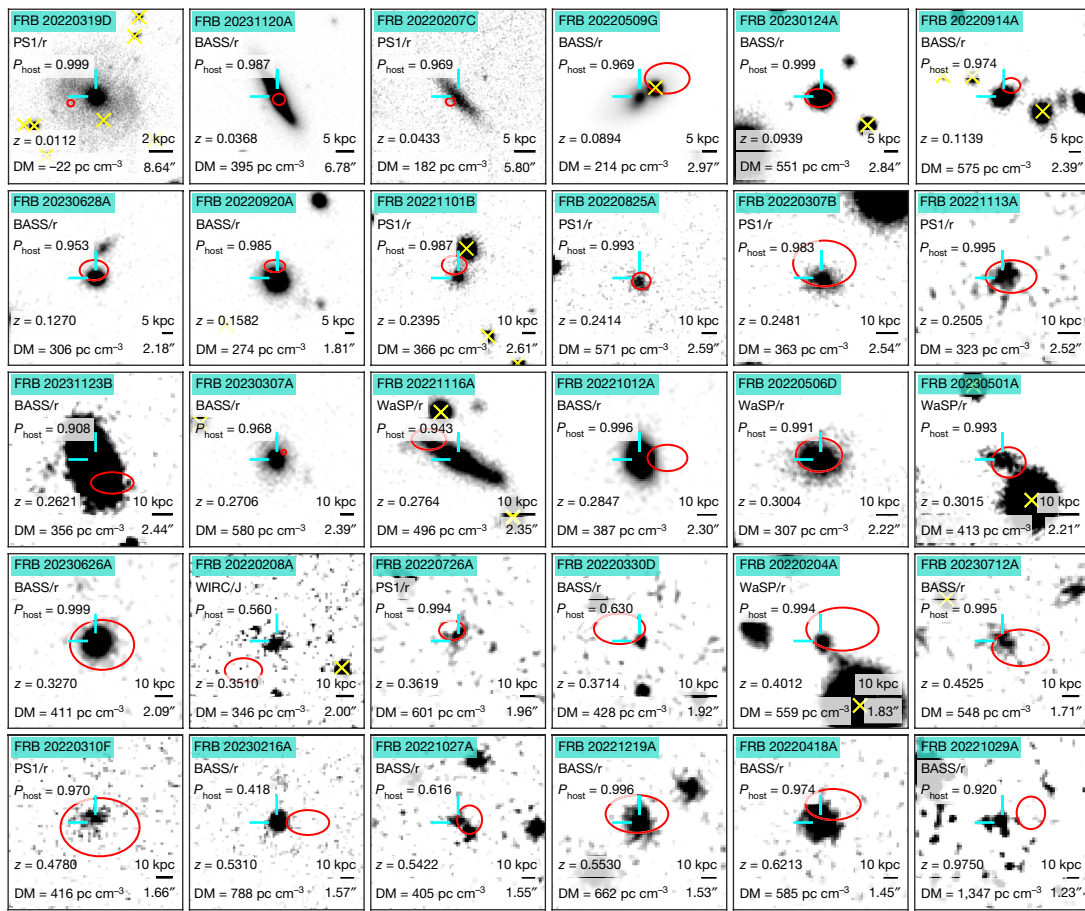


Fig. 1 | Optical/infrared imaging of the fields of FRBs discovered by the DSA-110. The images are centred on the PATH-identified host galaxies (cyan crosshairs) and panels are arranged in increasing order of redshifts (see Supplementary Table 1). The 90% confidence FRB localization regions are marked as red ellipses and stars are marked as yellow crosses. These images

reach 3σ depths of ≥ 23 – 24 mag and are oriented with north up and east to the left. The imaging instrument, association probability, extragalactic DM, redshift and physical scales are marked on the panels for reference. All images were smoothed with a Gaussian kernel of $\sigma = 0.15''$ to improve visibility.

We use the Bayesian Probabilistic Association of Transients to their Hosts (PATH) formalism¹⁹ on the deepest available imaging data to estimate the association probability (P_{host}) of the most likely host galaxy (see Methods). The PATH analysis finds secure host associations for 26 FRBs with $P_{\text{host}} \geq 90\%$ (see Extended Data Fig. 1). Of the remaining four events, FRBs 20221027A and 20220330D have two possible hosts, one of which is favoured by both the localizations and the DMs (see Methods). FRB 20230216A is found at a large offset from the preferred host, which lowers the association probability according to the chosen PATH setup, and the localization of FRB 20220208A is confused by the presence of a faint (23.4 mag in J-band data, spectroscopic redshift not available) alternative host. We further validate our host associations in Methods and Supplementary Figs. 3 and 4. We also discuss the hostless FRBs in Methods and Supplementary Fig. 5. The imaging mosaic of 30 FRB hosts included in our sample is shown in Fig. 1 (see Supplementary Fig. 6 for labelled axes) and the discovery properties of the host galaxies are tabulated in Supplementary Table 1. For all quantitative arguments in our work, we only consider secure host associations with $P_{\text{host}} \geq 90\%$.

Having identified the most probable host galaxies, we obtained optical spectroscopy with the Low Resolution Imaging Spectrometer (LRIS)²⁰ on Keck I, DEep Imaging Multi-Object Spectrograph (DEIMOS)²¹ on Keck II at the W. M. Keck Observatory and the Double Spectrograph (DBSP)²² on the 200-inch Hale Telescope at the Palomar Observatory (see Methods). The spectroscopic redshifts (z) and emission-line fluxes

are measured by jointly fitting the stellar continuum and nebular emission using the Penalized PiXel-Fitting (pPXF) software²³ (see Supplementary Fig. 7 and Supplementary Table 1). Next, we model the spectral energy distributions (SEDs) of the FRB host galaxies using the Prospector software²⁴, in which we jointly forward model the observed spectra, archival photometry from PS1, BASS, Mayall z-band Legacy Survey (MzLS)²⁵, Sloan Digital Sky Survey (SDSS)²⁶, Two Micron All Sky Survey (2MASS)²⁷, Wide-field Infrared Survey Explorer (WISE)²⁸ and Galaxy Evolution Explorer (GALEX)²⁹ surveys and photometry of data obtained with the WaSP and WIRC instruments (see Supplementary Table 3). We model the galaxies with a seven-component non-parametric star-formation history (SFH), a two-component dust attenuation model, a flexible dust attenuation curve, dust emission and a self-consistent nebular emission model (see Methods and Supplementary Table 4 for a summary of model parameters). Using standard empirical optical emission-line diagnostic diagrams^{30,31} (see Extended Data Fig. 2) and WISE colour-colour galaxy classifications³² (see Extended Data Fig. 3), we find that the dominant ionization mechanism in FRB host galaxies is consistent with the locus of star-forming galaxies (late-type spirals) and emission-line galaxies with active galactic nuclei (AGN, either LINERs or Seyferts) (see Methods and Supplementary Table 5). Therefore, we also include the emission from dust-enshrouded AGN in our SED modelling. The derived properties from our SED fits (see Supplementary Fig. 8) and constrained SFHs (see Supplementary Fig. 9) for FRB host galaxies are tabulated in Supplementary Table 6 and their distributions are shown in Extended Data Fig. 4.

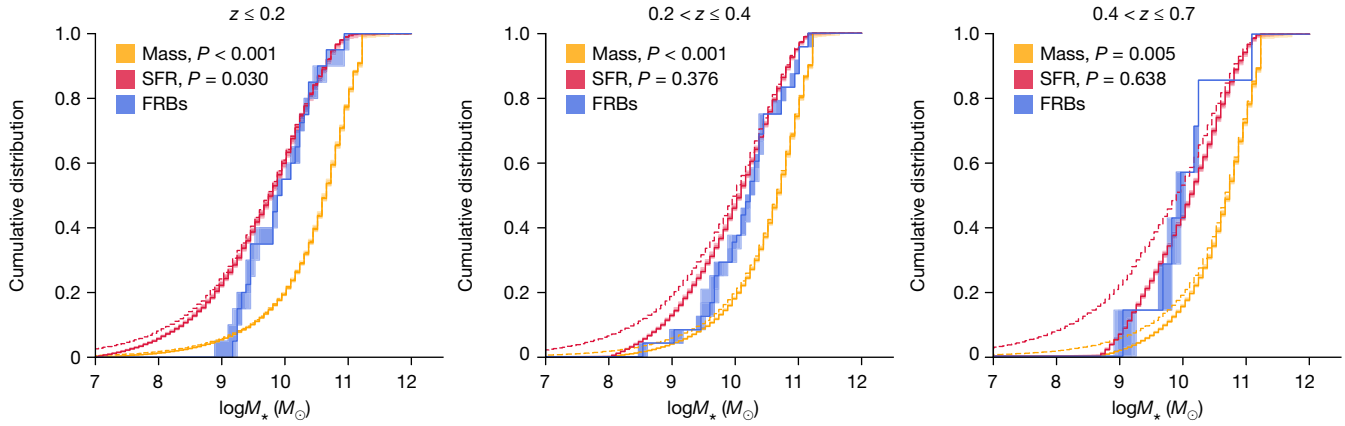


Fig. 2 | Comparison of FRB host galaxies with the distribution of galaxies in the Universe selected by stellar mass and star formation. We show cumulative distributions of galaxy stellar mass of samples selected in three ways: the occurrence of FRBs (blue), SFR (red) and stellar mass (orange). We correct the background stellar mass distributions for optical selection effects by using an r-band magnitude threshold of 23.5 mag (solid lines; see Methods). For reference, we also plot the distributions without this selection (dashed lines). The shaded regions represent the 1σ , 2σ and 3σ bands. Along with 26 secure host associations of DSA-110 FRBs from this work, we also include

samples of FRB host galaxies that follow our selection criteria^{4,5}. The distribution of FRB host stellar masses is inconsistent with the distribution of background galaxies selected by stellar mass in all redshift bins with $>3\sigma$ confidence. The P -value computed using the KS test for similarity with the distribution of background galaxies selected by SFR (red) is ≥ 0.01 in all redshift bins, indicating that the occurrence of FRBs is correlated with the occurrence of star formation. However, despite our sensitivity, there is a deficit of low-mass FRB hosts in the $z \leq 0.2$ bin.

To contextualize FRB host galaxies within the broader framework of star formation and stellar mass in the Universe, we compare them with the background galaxy population. In our comparison sample, alongside our 26 secure host associations, we include a complete literature sample of 26 FRB hosts^{4,5} that meet our selection criteria of r-band magnitude ≤ 23.5 mag and secure host association ($P_{\text{host}} \geq 90\%$). To address incompleteness inherent in magnitude-limited galaxy surveys, we used a hybrid approach to simulate the complete background galaxy population. We sample the galaxy stellar masses, M_* , from the stellar mass function, $\Phi(M_*, z)$ (ref. 33) and then compute the corresponding star-formation rate (SFR) using the star-forming main sequence (SFMS), $SFR(M_*, z)$ (ref. 34) and the distribution of galaxies in $\log M_* - \log SFR - z$ space³⁴ (see Methods and Supplementary Figs. 10 and 11). We compare the stellar mass distribution of FRB hosts with the distributions of stellar mass of background galaxies selected by two methods—weighted by SFR and weighted by stellar mass. We split the FRB comparison sample into three redshift bins to mitigate biases from the evolution of the background galaxy population: $z \leq 0.2$ with 20 FRBs, $0.2 < z \leq 0.4$ with 24 FRBs and $0.4 < z \leq 0.7$ with 7 FRBs. The lowest redshift bin edge was chosen on the basis of our capability to confidently identify low-mass galaxies, given the optical imaging depths (see Methods). Notably, FRB 20221029A was excluded from this analysis because of its solitary occurrence at $z \approx 1$, resulting in meaningful comparisons challenging at high redshifts owing to limited statistical power. We perform one-sample Kolmogorov–Smirnov (KS) tests between the sample of FRB stellar masses and the background distributions corrected for optical selection effect of r-band magnitude ≤ 23.5 mag (see Methods). The results are shown in Fig. 2.

We find that the sample of FRB host-galaxy stellar masses is inconsistent with the stellar mass distribution in the Universe but broadly consistent with the distribution of galaxies selected according to SFR. In all three redshift bins, the KS test P -value from the comparison between FRBs and galaxies selected according to stellar mass is < 0.001 (that is, $>3\sigma$ significance). Conversely, the comparison with the stellar mass distribution of galaxies selected according to SFR yields P -values greater than 0.01 in all the three redshift bins. This similarity to galaxies selected by SFR is further emphasized by the close alignment of FRB host galaxies with the SFMS of galaxies^{4,35} (see Extended Data Fig. 5). However, for $z \leq 0.2$, despite our sensitivity to optically faint

galaxies, we observe a notable scarcity of FRBs in the galaxies with $\log M_* \lesssim 9$ (see Fig. 2a). This is indicated by the low associated KS test result of $P = 0.030$; we note that the KS test is not optimal to quantify the importance of this claim. Radio selection effects are not expected to contribute to this scarcity of low-mass FRB hosts at $z \leq 0.2$ (ref. 36) (see Methods).

The dearth of $z \leq 0.2$ low-mass FRB host galaxies becomes even clearer when we compare them with host galaxies of the most prevalent class of CCSNe (Type II), which trace the occurrence of star formation in the Universe, with no dependence on other galaxy properties³⁷ (see Fig. 3b). We show the distribution of stellar masses of Type II CCSNe and FRB host galaxies in the r-band magnitude and redshift space in Fig. 3a. FRB hosts trace the locus of 0.1–1 L^* background galaxies and are more massive than typical Type II CCSNe host galaxies. To contextualize the rarity of the occurrence of Type II CCSNe in only massive galaxies on the scale of our $z \leq 0.2$ FRB sample size (N_{FRB}), we perform 1,000 Monte Carlo simulations in which we sample N_{FRB} galaxy stellar masses from the Type II CCSNe host distributions. We compute the fraction of these samples with all stellar masses above a particular stellar mass $\log M_*$ (see Extended Data Fig. 6). We find that, for our complete local universe FRB sample of size $N_{\text{FRB}} = 20$, the probability that all Type II CCSNe occur in galaxies more massive than $10^9 M_\odot$ is $P = 0.0014$ (3.2σ significance). If FRBs were an unbiased tracer of star formation in the Universe, then this quantifies the importance of the deficit of low-mass FRB hosts.

In contrast to previous studies suggesting that FRBs trace the occurrence of star formation in the Universe^{5,38}, we have shown that FRBs preferentially occur in massive star-forming galaxies and are a biased tracer of star formation in the Universe. This could point to an environment-dependent production efficiency of FRB sources. The primary driver of changes in stellar population properties with galaxy mass is the galaxy mass–metallicity relation⁸. Increased metallicity affects the evolution of massive stars by line-driven stellar winds, for which the mass-loss rate positively correlates with metallicity. Certain classes of supernova preferentially occur in low-metallicity environments³⁹, such as those that produce long-duration gamma-ray bursts (IGRBs) and superluminous supernovae (SLSNe)³⁷. We quantify the effect of metallicity on the selection of FRB host galaxies by constructing background stellar mass distributions weighted by SFR together

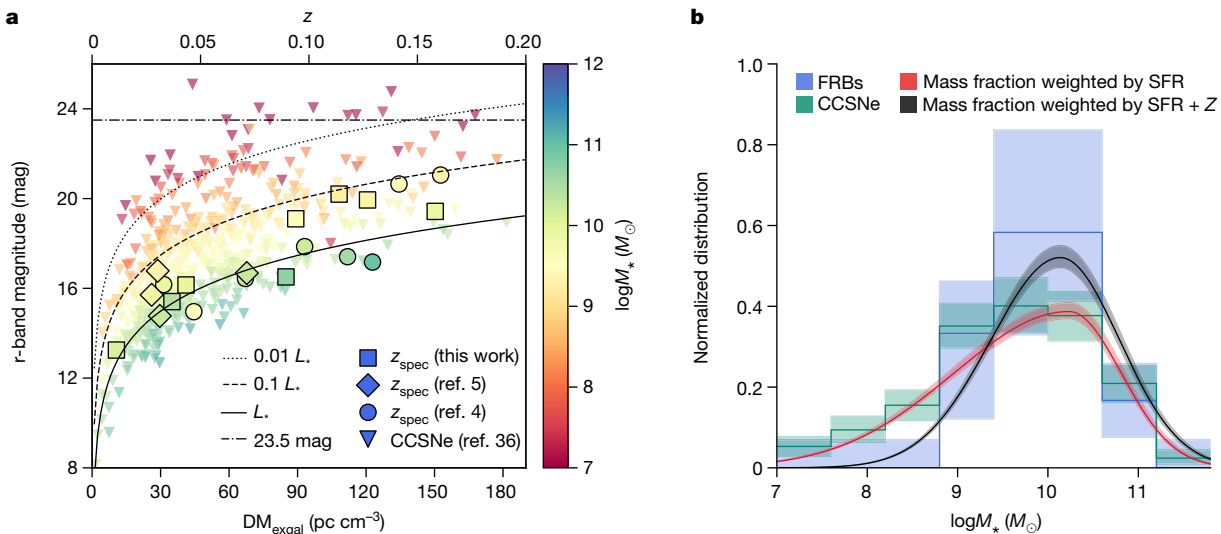


Fig. 3 | Investigation of whether FRBs trace star formation in the Universe using the $z \leq 0.2$ sample. **a**, Distribution of the r-band magnitude and redshift of FRB hosts published in this work (squares), alongside other FRB host-galaxy samples^{4,5} (circles and diamonds, respectively) with r-band magnitude ≤ 23.5 mag (dashed-dotted line) and $z \leq 0.2$. On comparing with the redshift evolution of galaxies with characteristic luminosities L_* (solid line), $0.1L_*$ (dashed line) and $0.01L_*$ (dotted line), we find that the FRB hosts trace approximately $0.1-1L_*$ galaxies. A comparison with the host galaxies of Type II CCSNe³⁷ (triangles) reveals that FRB host galaxies are relatively massive. **b**, This result

is also evident here, in which we show the host galaxy mass distributions (solid lines) with Poisson errors (shaded regions). Because Type II CCSNe (green) are unbiased tracers of star formation in the Universe, the SFR-weighted galaxy mass distribution (red) provides an adequate description of their host mass distribution. On the other hand, the host galaxies of FRBs (blue) show a clear dearth of low-mass galaxies. This absence can be accounted for by adding a metallicity-dependent FRB progenitor formation efficiency (black), which is stifled in environments with oxygen abundances, $12 + \log(\text{O/H}) \leq 8.08^{+0.61}_{-0.47}$, corresponding to a cutoff metallicity of $\log(Z/Z_\odot) = -0.61^{+0.61}_{-0.47}$.

with a metallicity-dependent FRB source formation efficiency $\rho = (1 + (-M/M_c)^\beta)^{-1}$. Here M_c is a characteristic cutoff mass that regulates the production of FRB sources, stopping their occurrence in lower-stellar-mass (and hence, lower-metallicity) galaxies and β regulates the strength of the metallicity cutoff. The best-fitting model suggests a strong cutoff with $\log M_c = 9.02$ (see Fig. 3b), thus implying that the formation efficiency of FRB sources is suppressed at oxygen abundances less than $12 + \log(\text{O/H}) \approx 8.08^{+0.61}_{-0.47}$, corresponding to a cutoff metallicity of $\log(Z/Z_\odot) = -0.61^{+0.61}_{-0.47}$. We determine this threshold metallicity by using the galaxy mass–metallicity relation⁸, which is incorporated as a prior in our SED modelling methodology (see Methods).

We have interpreted the preferential occurrence of FRBs in massive star-forming galaxies as a preference for high-metallicity environments, as inferred from the positive correlation between galaxy stellar mass and metallicity⁸. Magnetars are known to be potential FRB sources¹ and the preferential occurrence of FRBs in higher-metallicity environments may be expected in the scenario¹ that FRBs are emitted by magnetars formed in a sub-population of CCSNe. First, for single-star progenitors, elevated metallicity would favour the formation of neutron star remnants over black holes owing to increased mass loss in higher-metallicity stars⁴⁰. Further, stellar mergers have been theoretically demonstrated as the origin of magnetic blue straggler stars, which undergo rejuvenation by burning the accreted fuel from their companions and are believed to be potential progenitors of magnetars owing to the amplified magnetic fields of the merger remnants¹². The increase in the metallicity of intermediate-mass progenitor stars evolving in such binaries, which eventually culminate in CCSNe, increases the proportion of CCSNe occurring through this delayed binary evolution channel^{9,10}. The increased efficiency of CCSNe formation through binary interactions in high-metallicity settings probably arises from the association between metallicity and stellar size¹⁰. A star with higher metallicity is less compact as it evolves beyond the main sequence, thereby affecting the progression of mass transfer in binary systems⁴¹. At high metallicity, stars in binaries are more likely to evolve to fill their Roche lobes,

leading to unstable mass transfer and stellar mergers that potentially produce magnetar progenitors. A stellar-merger formation channel for magnetar progenitors may indeed be observationally favoured for the galactic magnetar population⁴².

We broaden our understanding of FRB sources by comparing the distributions of host-normalized projected galactocentric offsets and host galaxy stellar mass with various classes of transients (see Fig. 4 and Methods for a description of the literature samples used). We limit our comparisons to the local universe ($z \leq 0.2$) to potentially mitigate any unknown incompleteness that might be inherent to other transients at high redshifts. We also show the distribution for the entire redshift range in Extended Data Figs. 7 and 8. We correct the galaxy stellar mass distributions for the redshift evolution and perform two-sample KS tests to quantify the potential similarities (see Methods and Supplementary Table 7). In contrast to FRBs, the SLSNe and IGRBs predominantly manifest in the central star-forming regions of low-mass galaxies characterized by low metallicity and high specific SFR, thus highlighting the dissimilarities with FRBs. Although the offset distribution of ultraluminous X-ray (ULX) sources is consistent with FRBs ($P_{\text{KS}} = 0.09$), they demonstrate a preference for occurrence in massive galaxies and trace the background galaxy population selected by stellar mass and not star formation. The stellar mass distribution of FRB host galaxies is comparable with those of other classes of transient that trace star formation, including Type II CCSNe, Type Ia supernovae and short-duration gamma-ray bursts (sGRBs), but with the deficit of low-mass galaxies.

Some differences are apparent in the offset distributions of FRBs and classes of transients that trace star formation. Although FRBs are systematically found at larger offsets than Type II CCSNe and Type Ia supernovae, but smaller offsets than sGRBs, the host-normalized offsets are consistent with these three transient classes, owing to massive FRB host galaxies and the positive galaxy stellar mass–radius correlation. The larger absolute offset values may be a consequence of the radio-observation bias, in which bursts originating closer to the centre of star-forming spiral galaxies are overdispersed and exhibit

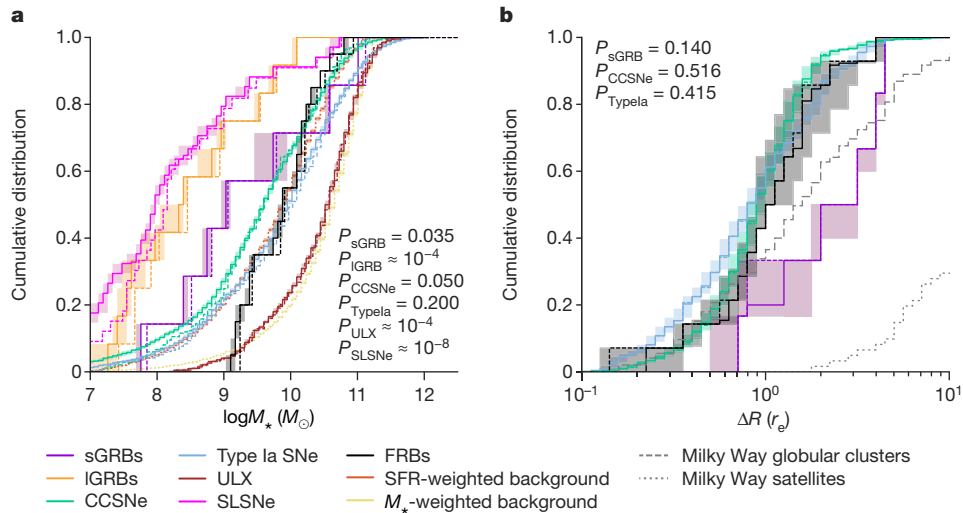


Fig. 4 | Comparison of FRB host galaxy properties with those of various transient classes at $z \leq 0.2$. We compare host galaxy stellar mass (a) and host-normalized galactocentric offset (b) distributions of FRBs with Type Ia supernovae (SNe), ultraluminous X-ray sources (ULX), superluminous supernovae (SLSNe), core-collapse supernovae (CCSNe), short-duration gamma-ray bursts (sGRBs) and long-duration gamma ray bursts (IGRBs) (see Methods for a description of the comparison samples). For comparisons, we only use our secure FRB host associations, together with the literature sample

of FRB host galaxies and offset measurements (see Methods). We correct stellar masses for redshift evolution⁴³ (see Methods). The measured values (dashed lines), median (thick lines) and 1σ errors (shaded regions) computed using 1,000 Monte Carlo samples of measurements reported in the literature are plotted. For reference, we also plot the background population selected by stellar mass (orange) and SFR (red) in panel a (see Fig. 2) and offsets of the satellites and globular clusters of the Milky Way in panel b.

higher scattering timescales³⁶, thus preventing their detection. If FRBs were to trace the locations of star formation within their host galaxies, this radio selection bias may shift the FRB offset distribution to lower offsets by up to about 1 kpc (ref. 43). On the other hand, the larger FRB offsets may be indicative of the long delays in CCSNe involving interacting binaries, which would imply that the CCSNe occur substantially displaced from the birth sites⁹. For example, if the typical stellar motions at the birth site are roughly 10 km s^{-1} and the delay time is 75 Myr, then the system would have drifted by 750 pc before the explosion. Alternatively, the larger offsets of FRBs may also arise from the contribution of non-CCSNe formation channels, such as the accretion-induced collapse or merger-induced collapse (AIC/MIC) of massive white dwarfs and binary neutron star mergers, towards FRB sources. The existence of these FRB source formation channels is indicated by the globular cluster FRB source 20201120E (refs. 44,45) and early DSA-110 results³⁵. To conclude, the larger offsets of FRBs may be because of either the delayed pre-CCSNe stellar merger magnetar formation scenario or contributions from non-CCSNe formation channels. However, we note that the current data show no evidence for the existence of several statistically different FRB host galaxy populations (see Methods).

Further insight into source formation channels may be gained through a detailed analysis of the distribution of FRB delay times with respect to the formation of their stellar progenitors⁴⁶. Non-CCSNe channels (for example, AIC/MIC of white dwarfs) are expected to have extended delay-time distributions of several billion years (ref. 47), whereas CCSNe of isolated stars occur on approximately 3–50-Myr stellar lifetimes and the CCSNe of stellar-merger remnants are expected to occur promptly within about 50–250 Myr of the birth of binary components⁹. The preferential occurrence of FRBs in massive star-forming galaxies is a constraint that applies to any model for FRB source formation. The influence of metallicity on the formation of FRB sources can be independently corroborated using forthcoming surveys. Given that star formation in the early Universe predominantly occurs within low-mass galaxies and galaxies of the same stellar mass at higher redshifts are less chemically enriched⁴⁸, the preference of FRBs for metal-rich environments implies a suppression of the proposed

FRB source formation channel at high redshifts. However, scenarios proposed for the repeating FRB 121102 (ref. 49), which is found in a low-metallicity dwarf-star-forming galaxy, may become more common at high redshifts. If most FRBs are emitted by magnetars such as those observed in the Milky Way, our results favour a scenario in which magnetars are generally formed from the CCSNe of stellar merger remnants in interacting binaries.

Online content

Any methods, additional references, Nature Portfolio reporting summaries, source data, extended data, supplementary information, acknowledgements, peer review information; details of author contributions and competing interests; and statements of data and code availability are available at <https://doi.org/10.1038/s41586-024-08074-9>.

1. Zhang, B. The physics of fast radio bursts. *Rev. Mod. Phys.* **95**, 035005 (2023).
2. CHIME/FRB Collaboration. A bright millisecond-duration radio burst from a Galactic magnetar. *Nature* **587**, 54–58 (2020).
3. Bochenek, C. D. et al. A fast radio burst associated with a Galactic magnetar. *Nature* **587**, 59–62 (2020).
4. Gordon, A. C. et al. The demographics, stellar populations, and star formation histories of fast radio burst host galaxies: implications for the progenitors. *Astrophys. J.* **954**, 80 (2023).
5. Bhardwaj, M. et al. Host galaxies for four nearby CHIME/FRB sources and the local universe FRB host galaxy population. *Astrophys. J. Lett.* **971**, L51 (2024).
6. Popov, S. B. in *Neutron Star Astrophysics at the Crossroads: Magnetars and the Multimessenger Revolution* Vol. 363 (eds Troja, E. & Baring, M. G.) 61–71 (Cambridge Univ. Press, 2023).
7. Kaspi, V. M. & Beloborodov, A. M. Magnetars. *Annu. Rev. Astron. Astrophys.* **55**, 261–301 (2017).
8. Gallazzi, A., Charlot, S., Brinchmann, J., White, S. D. M. & Tremonti, C. A. The ages and metallicities of galaxies in the local universe. *Mon. Not. R. Astron. Soc.* **362**, 41–58 (2005).
9. Zapartas, E. et al. Delay-time distribution of core-collapse supernovae with late events resulting from binary interaction. *Astron. Astrophys.* **601**, A29 (2017).
10. Zapartas, E. et al. The diverse lives of progenitors of hydrogen-rich core-collapse supernovae: the role of binary interaction. *Astron. Astrophys.* **631**, A5 (2019).
11. Frost, A. J. et al. A magnetic massive star has experienced a stellar merger. *Science* **384**, 214–217 (2024).
12. Schneider, F. R. N. et al. Stellar mergers as the origin of magnetic massive stars. *Nature* **574**, 211–214 (2019).
13. Weinreb, S. & Shi, J. Low noise amplifier with 7-K noise at 1.4 GHz and 25 °C. *IEEE Trans. Microw. Theory Tech.* **69**, 2345–2351 (2021).

14. Connor, L. et al. A gas rich cosmic web revealed by partitioning the missing baryons. Preprint at <https://arxiv.org/abs/2409.16952> (2024).
15. Chambers, K. C. et al. The Pan-STARRS1 surveys. Preprint at <https://arxiv.org/abs/1612.05560> (2016).
16. Zou, H. et al. Project overview of the Beijing–Arizona Sky Survey. *Publ. Astron. Soc. Pac.* **129**, 064101 (2017).
17. Nikzad, S. et al. High-efficiency UV/optical/NIR detectors for large aperture telescopes and UV explorer missions: development of and field observations with delta-doped arrays. *J. Astron. Telesc. Instrum. Syst.* **3**, 036002 (2017).
18. Wilson, J. C. et al. A wide-field infrared camera for the Palomar 200-inch telescope. *Proc. SPIE* **4841**, 451–458 (2003).
19. Aggarwal, K. et al. Probabilistic Association of Transients to their Hosts (PATH). *Astrophys. J.* **911**, 95 (2021).
20. Oke, J. B. et al. The Keck low-resolution imaging spectrometer. *Publ. Astron. Soc. Pac.* **107**, 375 (1995).
21. Faber, S. M. et al. The DEIMOS spectrograph for the Keck II Telescope: integration and testing. *Proc. SPIE* **4841**, 1657–1669 (2003).
22. Oke, J. B. & Gunn, J. E. An efficient low resolution and moderate resolution spectrograph for the Hale telescope. *Publ. Astron. Soc. Pac.* **94**, 586 (1982).
23. Cappellari, M. Full spectrum fitting with photometry in PPXF: stellar population versus dynamical masses, non-parametric star formation history and metallicity for 3200 LEGA-C galaxies at redshift $z = 0.8$. *Mon. Not. R. Astron. Soc.* **526**, 3273–3300 (2023).
24. Johnson, B. D., Leja, J., Conroy, C. & Speagle, J. S. Stellar population Inference with Prospector. *Astrophys. J. Suppl. Ser.* **254**, 22 (2021).
25. Dey, A. et al. Overview of the DESI Legacy Imaging Surveys. *Astron. J.* **157**, 168 (2019).
26. Alam, S. et al. The eleventh and twelfth data releases of the Sloan Digital Sky Survey: final data from SDSS-III. *Astrophys. J. Suppl. Ser.* **219**, 12 (2015).
27. Skrutskie, M. F. et al. The Two Micron All Sky Survey (2MASS). *Astron. J.* **131**, 1163–1183 (2006).
28. Cutri, R. M. et al. VizieR Online Data Catalog: AllWISE Data Release (Cutri+ 2013). *VizieR Online Data Catalog II/328* (2021).
29. Martin, D. C. et al. The Galaxy Evolution Explorer: a space ultraviolet survey mission. *Astrophys. J. Lett.* **619**, L1–L6 (2005).
30. Baldwin, J. A., Phillips, M. M. & Terlevich, R. Classification parameters for the emission-line spectra of extragalactic objects. *Publ. Astron. Soc. Pac.* **93**, 5–19 (1981).
31. Kewley, L. J., Groves, B., Kauffmann, G. & Heckman, T. The host galaxies and classification of active galactic nuclei. *Mon. Not. R. Astron. Soc.* **372**, 961–976 (2006).
32. Wright, E. L. et al. The Wide-field Infrared Survey Explorer (WISE): mission description and initial on-orbit performance. *Astron. J.* **140**, 1868–1881 (2010).
33. Leja, J. et al. A new census of the $0.2 < z < 3.0$ universe. I. The stellar mass function. *Astrophys. J.* **893**, 111 (2020).
34. Leja, J. et al. A new census of the $0.2 < z < 3.0$ universe. II. The star-forming sequence. *Astrophys. J.* **936**, 165 (2022).
35. Law, C. J. et al. Deep Synoptic Array science: first FRB and host galaxy catalog. *Astrophys. J.* **967**, 29 (2024).
36. Ocker, S. K., Cordes, J. M., Chatterjee, S. & Gorsuch, M. R. Radio scattering horizons for galactic and extragalactic transients. *Astrophys. J.* **934**, 71 (2022).
37. Schulze, S. et al. The Palomar Transient Factory core-collapse supernova host-galaxy sample. I. Host-galaxy distribution functions and environment dependence of core-collapse supernovae. *Astrophys. J. Suppl. Ser.* **255**, 29 (2021).
38. James, C. W. et al. The fast radio burst population evolves, consistent with the star formation rate. *Mon. Not. R. Astron. Soc.* **510**, L18–L23 (2022).
39. Taggart, K. & Perley, D. A. Core-collapse, superluminous, and gamma-ray burst supernova host galaxy populations at low redshift: the importance of dwarf and starbursting galaxies. *Mon. Not. R. Astron. Soc.* **503**, 3931–3952 (2021).
40. Heger, A., Fryer, C. L., Woosley, S. E., Langer, N. & Hartmann, D. H. How massive single stars end their life. *Astrophys. J.* **591**, 288–300 (2003).
41. Klencki, J., Nelemans, G., Istrate, A. G. & Pols, O. Massive donors in interacting binaries: effect of metallicity. *Astron. Astrophys.* **638**, A55 (2020).
42. Sherman, M. B. et al. Searching for magnetar binaries disrupted by core-collapse supernovae. *Mon. Not. R. Astron. Soc.* **531**, 2379–2414 (2024).
43. Seebeck, J. et al. The effects of selection biases on the analysis of localised fast radio bursts. Preprint at <https://arxiv.org/abs/2112.07639> (2021).
44. Bhardwaj, M. et al. A nearby repeating fast radio burst in the direction of M81. *Astrophys. J. Lett.* **910**, L18 (2021).
45. Kremer, K., Piro, A. L. & Li, D. Dynamical formation channels for fast radio bursts in globular clusters. *Astrophys. J. Lett.* **917**, L11 (2021).
46. Sharma, K. et al. Deep Synoptic Array science: a massive elliptical host among two galaxy-cluster fast radio bursts. *Astrophys. J.* **950**, 175 (2023).
47. Tauris, T. M., Sanyal, D., Yoon, S. C. & Langer, N. Evolution towards and beyond accretion-induced collapse of massive white dwarfs and formation of millisecond pulsars. *Astron. Astrophys.* **558**, A39 (2013).
48. Ma, X. et al. The origin and evolution of the galaxy mass–metallicity relation. *Mon. Not. R. Astron. Soc.* **456**, 2140–2156 (2016).
49. Margalit, B. & Metzger, B. D. A concordance picture of FRB 121102 as a flaring magnetar embedded in a magnetized ion-electron wind nebula. *Astrophys. J. Lett.* **868**, L4 (2018).

Publisher's note Springer Nature remains neutral with regard to jurisdictional claims in published maps and institutional affiliations.

Springer Nature or its licensor (e.g. a society or other partner) holds exclusive rights to this article under a publishing agreement with the author(s) or other rightsholder(s); author self-archiving of the accepted manuscript version of this article is solely governed by the terms of such publishing agreement and applicable law.

© The Author(s), under exclusive licence to Springer Nature Limited 2024

Methods

The DSA-110 instrument and FRB localizations

All DSA-110 FRBs presented here were detected between February 2022 and November 2023 with a limited array of 48 core antennas and 15 outriggers⁵⁰. Here we summarize details of the FRB detection system and localization procedures.

The DSA-110 is a radio interferometer operating between 1,311 and 1,499 MHz with 4.65-m dish antennas. The antennas have an automatic elevation drive enabling repointing along the meridian and are equipped with dual linearly polarized receivers and ambient-temperature low-noise amplifiers delivering a system temperature of 25 K (ref. 13). A coherent real-time search for FRBs over approximately 14 deg² is implemented using the core antennas, which are evenly spaced along a 400 m east–west infrastructure. During the observations presented here, the array was primarily pointed at a declination of 71.6°. We use a modified version of heimdall⁵¹ software to perform the search on total intensity data in 256 fan-shaped beams spaced by 1 arcmin perpendicularly to the meridian. The data are integrated over 262.144 μs and channelized into 768 244.14-kHz channels. We search for FRBs with boxcar time-domain filters between 1 and 32 times the minimum time resolution and between DMs of 75% of the galactic expectation from the NE2001 model and 1,500 pc cm⁻³. Triggered FRB events prompt the storage of 4-bit voltage data from the core and outrigger antennas (maximum baseline of 2.5 km) for 61,440 samples at 32.768-μs time resolution in 6,144 × 30.518-kHz channels. Furthermore, we store 4 h of visibility data near the trigger time.

We derive arcsecond-scale localizations using the triggered voltage-data dumps, combined with slower-cadence visibilities recorded over 4 h surrounding each FRB and 5 min of visibility data on the bandpass-calibrator source 3C309.1 obtained within 12 h of each FRB. For each FRB, we form the following datasets as Common Astronomy Software Applications (CASA) software⁵² (version 5.4.1) measurement sets (MSs).

- A 5-min bandpass-calibrator MS with 3C309.1 at the phase centre. This MS is formed using data obtained when 3C309.1 transits through the centre of the primary beam. We assume a flux density of 7.6 Jy for 3C309.1, based on the VLA Calibrator Manual. This assumption is not critical to the analysis but is useful in some verification steps described below.
- 5-min MSs recorded during the transits of between 8 and 18 Very Long Baseline Interferometry (VLBI) calibrator sources observed within ±2 h of the FRB. VLBI calibrators are selected from the 2022b Radio Fundamental Catalog as sources with flux densities >50 mJy, located within ±1.3° of the pointing declination.
- A 10-min MS containing data in the FRB field, formed using data temporally centred on the FRB detection. These data are phased to the pointing centre at the time of the FRB detection.
- A 1.1-s MS formed by correlating the triggered voltage dump, phased to the pointing centre at the time of the FRB detection.
- A MS with a single integration formed by dedispersing and correlating the triggered voltage dump and integrating only the data containing the FRB. The optimal FRB DM is used for dedispersion.

Our calibration and imaging procedure is then as follows.

- We remove frequency channels affected by radio-frequency interference in all data through visual inspection. We also remove baselines to any malfunctioning antennas.
- We then use the CASA task ‘bandpass’ to derive an antenna-based complex bandpass from the 3C309.1 data. In all analyses, we exclude baselines shorter than 45 m, as these are affected by spurious correlations owing to cross-talk and low-level radio-frequency interference. This solution is applied to every other dataset. Any ‘delay’ terms are absorbed into the complex bandpass.

- We use the wsclean software⁵³ to generate a 3.3° image from the 10-min FRB-field MS. Standard w -projection is applied. We verify that >95% of compact (<20 arcsec major axes), bright (>20 mJy) sources in the NRAO VLA Sky Survey (NVSS)⁵⁴ catalogue are detected with approximately the correct flux densities in this image. This is occasionally not the case, which we attribute to poor calibration, and we then perform a phase-only gain calibration using a sky model derived from the NVSS. The model includes all sources within the primary beam modelled as elliptical Gaussians. This second calibration is applied to all data if necessary.
- We then use wsclean to make 5.5° images of the FRB MS and the 1.1-s voltage MS, and small 0.17° images of each VLBI calibrator MS. The small images in particular have pixel sizes of 0.3 arcsec to enable accurate image-plane astrometry.
- We verify that extremely bright (>400 mJy) continuum sources from the NVSS are detected in the image made from the 2-s voltage MS, at approximately the correct positions. This is a basic check for valid voltage data and associated correlation products.
- We manually identify the approximate FRB position to within a few arcseconds in the large image of the FRB MS, using the location of the detection beam as a guide and checking that it is undetected in the voltage MS image. We then use the CASA task ‘tclean’ to make a small image (0.17°, 0.3-arcsec pixels) with the approximate FRB position as the phase centre and fit the FRB position in the image plane. We measure the signal-to-noise (S/N) ratio, σ_{FRB} , of the FRB in the image plane and, using the full width at half maxima of the synthesized beam in right ascension and declination (s_θ and s_ϕ , respectively), we derive the statistical localization uncertainty as $0.45 \times s_{\theta,\phi}/\sigma_{\text{FRB}}$.
- We fit the derived positions of each VLBI calibrator using their associated images and perform a weighted (according to the image S/N) linear-model fit to the right ascension and declination position offsets with time. We correct the FRB position by the predicted image offsets at the burst detection time and add the formal uncertainty in this prediction in quadrature to the statistical localization uncertainty. Typical corrections are at the sub-arcsecond level, with maximum observed corrections of about 2 arcsec. This method is physically motivated by the fact that the DSA-110 array essentially fits entirely within a physical correlation length in the case of ionospheric path-length errors, such that the errors can be modelled as bulk astrometric shifts.

Given the reliance of this work on accurate FRB localizations, we performed and present here an end-to-end test of the procedure. We analysed 35 archived voltage dumps obtained in a variety of observing conditions during the year 2023, including on FRBs and pulsars. In these datasets, we identified 69 continuum sources selected from the NVSS catalogue with flux densities >400 mJy, major axes <35 arcsec and locations within 2.1° of the primary-beam centre. For such bright sources, the NVSS catalogue positions have uncertainties of approximately 0.5 arcsec in right ascension and 0.6 arcsec in declination⁵⁴. Using exactly the same procedures as for the FRBs, we determined the position of each source in the DSA-110 data using 1.1 s of voltage data and a random DM between 80 and 1,500 pc cm⁻³. The sources were detected with S/N ratios between 8 and 20.

In Supplementary Fig. 1, we show the offsets of the derived continuum-source positions from the NVSS catalogue positions and the uncertainties in the derived positions. Just as for the FRBs, the localization uncertainties are the quadrature sums of the theoretical statistical uncertainties given the image S/N and the uncertainties in the final astrometric corrections from the adjacent VLBI calibrator sources. We find that only 4/69 of the 90% confidence error ellipses do not contain the true source positions, consistent with expectations. We also do not find any notable systematic biases in the derived positions.

Finally, we address an issue with the published DSA-110 localization of FRB 20220912A (ref. 50), identified by Hewitt et al.⁵⁵. The DSA-110 90% confidence localization ellipse was found to be approximately

Article

0.6 arcsec offset from the correct VLBI position. We attribute this error to poorly converged in-field calibration solutions and the fact that we had not yet incorporated astrometric corrections derived from adjacent VLBI calibrators into the localization procedure. We reprocessed the DSA-110 data on the 18 October 2022 burst from FRB 20220912A using the methods described above and derived a revised burst position of (J2000) RA = 23 h 09 min 04.83 s, dec. = +48 d 42 min 23.6 s, with uncertainties (1σ) of ± 1.3 arcsec in right ascension and ± 0.9 arcsec in declination (see Supplementary Fig. 2). This position is consistent with the results of ref. 55.

Next we discuss the possibility of any selection biases from the DM cut of $1,500 \text{ pc cm}^{-3}$ used in our FRB search pipeline. Essentially, a DM cut of $1,500 \text{ pc cm}^{-3}$ excludes FRB hosts under two scenarios: either the FRBs are very distant or the FRBs have excess local DM. In the first scenario, assuming a median host DM contribution of $\text{DM}_{\text{host}} = 120 \text{ pc cm}^{-3}$ (ref. 14) and attributing the remaining DM to the diffuse baryons in the intergalactic medium (IGM), the expected host galaxy redshift for DM_{IGM} of $1,380 \text{ pc cm}^{-3}$, based on the $\text{DM}_{\text{IGM}} - z$ relation⁵⁶, is $z = 1.51^{+0.17}_{-0.38}$. Because our analysis includes only FRBs, background galaxies and other transients at $z \leq 1$, this suggests that limiting our sample to a DM of $1,500 \text{ pc cm}^{-3}$ does not introduce substantial biases. In the second scenario, assuming a log-normal host galaxy DM distribution with $\mu = 4.8$ and $\sigma = 0.5$ (ref. 14), we evaluate the likelihood of a FRB with $\text{DM} > 1,500 \text{ pc cm}^{-3}$ occurring in host galaxies at lower redshifts. For a $\text{DM}_{\text{exgal}} = 1,500 \text{ pc cm}^{-3}$, the probabilities that the FRB has excess local DM and is associated with a host galaxy at various redshifts are: $P(\text{DM}_{\text{host}} > \text{DM}_{\text{exgal}} - \langle \text{DM}_{\text{IGM}}(z=0.2) \rangle) = 9.5 \times 10^{-7}$ at $z \leq 0.2$, $P(\text{DM}_{\text{host}} > \text{DM}_{\text{exgal}} - \langle \text{DM}_{\text{IGM}}(z=0.4) \rangle) = 3.7 \times 10^{-6}$ at $z \leq 0.4$, $P(\text{DM}_{\text{host}} > \text{DM}_{\text{exgal}} - \langle \text{DM}_{\text{IGM}}(z=0.7) \rangle) = 4 \times 10^{-5}$ at $z \leq 0.7$ and $P(\text{DM}_{\text{host}} > \text{DM}_{\text{exgal}} - \langle \text{DM}_{\text{IGM}}(z=1) \rangle) = 6.8 \times 10^{-4}$ at $z \leq 1$. These probabilities indicate that the occurrence of a FRB with $\text{DM} > 1,500 \text{ pc cm}^{-3}$ in host galaxies at lower redshifts is highly unlikely. Thus, it is evident that our sample is not substantially affected by selection biases owing to the DM cut of $1,500 \text{ pc cm}^{-3}$.

FRB host association and sample selection

The FRBs published in this work were selected such that there is a plausible candidate host galaxy in the vicinity of the localization region detected in either PS1 (ref. 15) or the BASS¹⁶ from the Dark Energy Survey⁵⁷ r-band data. Out of 42 FRBs discovered by the DSA-110 during its science commissioning phase from February 2022 to November 2023, 30 FRBs had a plausible candidate host galaxy. In cases of marginal optical detections, we obtain deeper imaging in our follow-up campaigns. We then use the Bayesian PATH formalism to identify the host galaxy and estimate its probability of association¹⁹. This formalism invokes Bayes' rule to calculate the posterior probability $P(O_i|x)$, in which O_i is the case that the FRB is from galaxy i and x represents the observables, such as FRB localization, galaxy coordinates, magnitude and angular size.

We use galactic extinction-corrected r-band magnitudes for our PATH analysis, unless deeper imaging in another band is available (see Supplementary Table 1 for a summary of optical/infrared imaging used for PATH analysis). When the deepest available imaging is PS1 or BASS r-band, we use their respective published source catalogues to identify the set of candidate host galaxies within $30''$ of the localization. For PS1, we query VizieR⁵⁸ using Astropy^{59,60} and remove point sources using the PS1 Point Source Catalog⁶¹ queried using CasJobs⁶². For the BASS, we extract the DR9 source catalogue from Legacy Survey Browser⁶³ and identify galaxy candidates using the Tractor morphological classifications. We use the catalogued half-light radii and photometry in our PATH analysis. For FRB fields with deeper imaging from our follow-up campaigns, we obtain the astrometry solution using Astrometry.net⁶⁴. We use SExtractor⁶⁵ to extract all $\geq 2\sigma$ sources in the field and remove point sources using the CLASS_STAR classifier with an 85% threshold. The source magnitudes are calibrated by correcting for zero points computed by

cross-matching SExtractor-identified sources with the # II/349/ps1 catalogue⁶⁶. The half-light radii are measured by iteratively fitting elliptical isophotes using standard procedures defined in photutils⁶⁷.

The key observables in our analysis include the candidate host magnitude (m), host-normalized offsets (θ/ϕ) and the probability of non-detection of the host galaxy owing to limited imaging depth $P(U)$. We assume that the brighter candidate galaxies have a higher prior probability, $P(O_i) \propto \frac{1}{\Sigma(m_i)}$, in which $\Sigma(m_i)$ is the angular surface density of galaxies on the sky with magnitude $m \leq m_i$. Because the true angular distribution of FRBs is unknown, we assume an exponential host-normalized offset distribution (θ/ϕ) and assert a maximum offset of $\theta_{\max} = 6\phi$. Although quantifying $P(U)$ is tricky, incorporating the probability of host invisibility in optically limited data has crucial implications on (but not limited to) offsets and host galaxy properties distributions. We use $P(U) = 0.2$ for PS1 and $P(U) = 0.1$ for deeper BASS, WIRC and WaSP imaging based on tests with simulated FRB populations⁴³.

We perform PATH analysis on the deepest available images of FRB fields using the procedure outlined above (see Fig. 1 for images). The PATH analysis confidently associates 26 out of 30 FRBs to a host galaxy with $P(O_i|x) \geq 90\%$. The distribution of PATH association probabilities in the $m - \theta/\phi$ space of observables in Extended Data Fig. 1 indicates that the four FRBs with insecure host associations are the ones with typically fainter hosts and at higher host-normalized offsets, assuming the most likely host. We investigate the cause of lower host association probabilities for these four FRBs further. FRB 20230216A has an $m = 21.4$ mag host candidate at host-normalized offset of $\theta/\phi = 5.4$. As this angular offset is very close to the maximum offset permitted by our PATH priors $\theta_{\max} = 6\phi$, the association probability of this candidate host is low ($P(O_i|x) = 0.42$). FRB 20220208A had an $m = 20.8$ mag secure host galaxy in PS1 r-band image with $P(O_i|x) = 0.98$. However, deeper imaging revealed another faint candidate host galaxy with $m = 23.4$ mag in the WIRC J-band image, which lowered the association probability of the PS1 host candidate to $P(O_i|x) = 0.56$. FRB 20220330D had an $m = 22.5$ mag secure host galaxy in the BASS r-band image with $P(O_i|x) = 0.94$. We noticed another faint source with $m = 23.4$ mag in the vicinity of the localization region, which Tractor morphological classifications identified as a star. We obtained a spectrum of this source and identified it as a misclassification in Legacy catalogues. Incorporating this galaxy in our PATH analysis identified it as the most probable host galaxy with $P(O_i|x) = 0.63$. The host association probability of FRB 20221027A is low ($P(O_i|x) = 0.62$) because it has two candidate host galaxies in the BASS with $m = 22.1$ mag and $m = 22.8$ mag, respectively. We investigate the cases of FRB 20220330D and FRB 20221027A further by obtaining the redshift of the second-likely host (z_2) and comparing the $P(z|\text{DM}_{\text{exgal}})$ for the two candidates computed using a standard $\text{DM}_{\text{IGM}} - z$ relation⁵⁶. For FRB 20221027A, $P(z_1 = 0.542|\text{DM}_{\text{exgal}}) = 0.758$ and $P(z_2 = 0.229|\text{DM}_{\text{exgal}}) = 0.242$ and for FRB 20220330D, $P(z_1 = 0.371|\text{DM}_{\text{exgal}}) = 0.634$ and $P(z_2 = 0.671|\text{DM}_{\text{exgal}}) = 0.366$, in which the subscript '1' denotes the PATH-identified host. Because in both cases the DM_{exgal} considerations also prefer the host identified by PATH analysis, we declare them as the most likely host. As the other candidate host of FRB 20220208A is very faint ($m = 23.4$ mag in J band), we refrain from obtaining its redshift owing to limited observational resources.

Validating our host associations

We validate the DSA-110 FRB host associations using the following three-step methodology. First, we show that, with the localization capabilities and optical imaging depths of the DSA, we confidently associate FRBs with low-mass galaxies at low redshifts ($z \lesssim 0.2$), strengthening our result of the deficit of low-mass galaxies. Second, for higher redshifts, we quantify the rarity of the presence of a luminous galaxy along the FRB sight line using the probability of chance coincidence to justify these associations. Third, we reject the hypothesis of another low-luminosity host galaxy along the FRB sight line by quantifying the improbability

of more than one galaxy existing within the cosmic volume defined by the localization region and the extragalactic DM of the FRB. Next, we discuss these points in detail.

Robust host galaxy associations at low redshifts, considering the localization capabilities of the DSA-110 and the optical imaging depth of the surveys used. The robustness of FRB host galaxy associations is a function of FRB localization area from the radio interferometer and the limiting magnitude of the optical imaging surveys⁶⁸. To assess the extent of our proficiency in confidently associating a FRB to a low-mass galaxy, we perform the following simulation. For r-band magnitudes in the range $m \in [12, 26]$ mag and redshifts in the range $z \in [0, 1.2]$, we compute the galaxy stellar mass (M_*) assuming mass-to-light ratio $M_*/L_* = 1$. We then compute the representative host galaxy half-light radius (R_h) for a galaxy of stellar mass M_* using the mass-radius correlation of late-type galaxies⁶⁹. We compute the probability of chance coincidence (P_{cc}) using galaxy number counts for apparent r-band magnitudes. We follow the methodology in ref. 68 and fit the r-band galaxy number counts in ref. 70 to compute the projected areal number density of galaxies brighter than r-band magnitude, $\sigma(\leq m)$. We then compute the P_{cc} of occurring within a radius R , assuming a Poisson distribution of galaxies across the sky as

$$P_{cc} = 1 - \exp^{-\pi R^2 \sigma(\leq m)}, \quad (1)$$

in which R is parameterized as $R = \max(2R_{\text{FRB}}, \sqrt{R_0^2 + 4R_h^2})$, where R_{FRB} is the equivalent radius that corresponds to 1σ of the localization area, R_0 is the radial angular separation between the FRB position and a presumed host and R_h is the half-light radius. Typical 1σ localization uncertainty of DSA-110 is $\lesssim 2''$. For the purpose of testing our host association capabilities and to put upper limits on the P_{cc} , we use $R_0 \approx 2R_h$ and $R_{\text{FRB}} = 3''$ in our simulation. The results of this simulation are shown in Supplementary Fig. 3a. We observe that, in the absence of any optical observation biases, the DSA-110 localizations are sufficient to confidently associate FRBs to their true host galaxies. The FRBs can be associated to their true low-mass $0.01\text{--}0.1 L_*$ galaxies with $P_{cc} \lesssim 0.1$. However, the optical observation bias of r-band magnitude $\lesssim 23.5$ mag limits our ability to associate FRBs to low-mass galaxies at high redshifts. Nonetheless, at low redshifts ($\lesssim 0.2$), the optical observation biases barely affect our host associations and we are capable of confidently associating FRBs to low-mass $0.001\text{--}0.1 L_*$ galaxies with $P_{cc} \lesssim 0.1$. This implies that our host associations at $z \lesssim 0.2$ are robust.

Rarity of existence of a massive galaxy within the small DSA-110 localization region. The probability of chance coincidence also quantifies the rarity of existence of a massive galaxy within the localization uncertainty of the FRB by virtue of the fact that massive galaxies in the Universe are rare compared with the low-mass galaxies and the probability of chance existence of a massive galaxy within the small DSA-110 localization area is small. Motivated by this, we compute the P_{cc} for all DSA-110 FRBs and plot them in Supplementary Fig. 3b in the space of their characteristic radius (a function of R_{FRB} , R_0 and R_h) and r-band magnitude. We observe that the probability of chance occurrence of our FRBs along a sight line close to these massive galaxies is smaller than 0.1, thus strengthening our associations.

Rarity of existence of several candidate galaxies within the cosmic volume permitted by DSA-110 localization uncertainties and FRB DM. We begin by computing the average number density of galaxies in the Universe³³ (n) as a function of redshift (z), while also accounting for galaxy clustering⁷¹. First, we compute the stellar mass function of the galaxies³³ $dn(z)/d\log M$. To compute the total number density of galaxies, we integrate this mass function in the range $\log M \in [5, 12]$, in which the lower limit is set on the basis of the lowest-mass CCSNe host galaxy³⁷. Because the distribution of galaxies in the

low-redshift Universe is non-homogeneous, we account for galaxy clustering⁷¹ to compute the effective galaxy number density (n_{eff}) in the redshift slice z to $z + dz$ as

$$n_{\text{eff}}(z) = n(z) \frac{\int_0^\Delta (1 + \xi(r)) r^2 dr}{\int_0^\Delta r^2 dr}, \quad (2)$$

in which Δ is the thickness of the comoving shell between redshifts z and $z + dz$ and $\xi(r)$ is the two-point correlation function that describes the excess probability, compared with a random distribution, of finding a pair of galaxies separated by a distance r ,

$$\xi(r) = \left(\frac{r}{r_0} \right)^{-\gamma}, \quad (3)$$

in which $\gamma \approx 1.8$ is the power-law index⁷¹ and r_0 is the characteristic correlation length⁷¹, $r_0 = 5.4 \text{ h}^{-1} \text{ Mpc}$. Having computed the effective galaxy number density (n_{eff}), we compute the expected number of galaxies as $N_{\text{eff}} = n_{\text{eff}} \times V_{\text{loc},z}$, in which $V_{\text{loc},z}$ is the conical shell volume defined by the localization uncertainties and redshift slice z to $z + dz$, computed as

$$V_{\text{loc},z} = \frac{\Omega}{4\pi} \times \frac{4\pi}{3} (D_c(z+dz)^3 - D_c(z)^3), \quad (4)$$

in which Ω is the solid angle of the conical region computed as $\Omega = \pi \theta^2 D_A(z)^2 / D_c(z)^2$, in which we use double the maximum localization uncertainties, $\theta = 6''$, to present a conservative estimate on galaxy counts, $D_A(z)$ is the angular diameter distance and $D_c(z)$ is the comoving distance at redshift z . We plot $N_{\text{eff}}(z)$ in Supplementary Fig. 4a for reference. We also include uncertainties on $N_{\text{eff}}(z)$, which primarily arise from the uncertainties on the mass function.

Next, we compute the average number of galaxies within the localization region ($\bar{N}(\text{DM})$), given the FRB DM. To this end, for FRB extragalactic DM_{exgal} $\in [0, 1,000]$ pc cm⁻³, we first compute $P(z|\text{DM}_{\text{exgal}})$ by assuming that the extragalactic DM is attributed to diffuse baryons in the IGM⁵⁶. We then compute $\bar{N}(\text{DM})$ as follows,

$$\bar{N}(\text{DM}_{\text{exgal}}) = \int_0^2 N_{\text{eff}}(z) \times P(z|\text{DM}_{\text{exgal}}) dz. \quad (5)$$

Finally, we run the following simulation to compute $P(\text{galaxy counts} > 1|\text{DM}_{\text{exgal}})$. For each DM_{exgal} , we sample 10,000 galaxy counts from a Poisson distribution with the mean $\bar{N}(\text{DM}_{\text{exgal}})$ and then compute $P(\text{galaxy counts} > 1|\text{DM}_{\text{exgal}})$ as the fraction of these samples for which the counts are greater than 1. We run this in a Monte Carlo simulation to also compute the uncertainties on the probabilities. We plot our results in Supplementary Fig. 4b.

We find that, for $\text{DM}_{\text{exgal}} \lesssim 200$ pc cm⁻³, the probability of existence of more than one galaxy within 6'' of the localization is $\lesssim 0.20^{+0.04}_{-0.04}\%$. Most DSA-110 FRBs have $\text{DM}_{\text{exgal}} \lesssim 600$ pc cm⁻³, implying a probability of existence of more than one galaxy $\lesssim 2.00^{+0.14}_{-0.14}\%$. For increasing DM_{exgal} , this probability increases to a maximum value of $2.93^{+0.17}_{-0.17}\%$, primarily because of the larger cosmic volume examined by the localization region. Therefore, the maximum probability of existence of more than one galaxy within 6'' of DSA-110 FRB localizations is approximately 3%. This implies that, out of 30 DSA-110 FRBs, we expect a confusion between more than one candidate host galaxy for at most $30 \times 0.03 \approx 1$ case, thus quantifying the rarity of this scenario.

For completeness, we also quantify the rarity of existence of more than one galaxy within 6'' of the localization by following another methodology. For a given FRB extragalactic DM, we estimate redshift upper limits, z_{max} , assuming that DM_{exgal} is attributed to diffuse baryons in the IGM and using the $\text{DM}_{\text{IGM}} - z$ relation⁵⁶. We estimate these redshift upper limits (z_{max}) by computing the redshift corresponding to the

Article

95th percentile of the probability distribution, $P(z|\text{DM}_{\text{exgal}})$. We then compute the mean number of galaxies within the comoving volume out to redshift z_{max} as

$$\bar{N}(\text{DM}_{\text{exgal}}) = \int_0^{z_{\text{max}}} N_{\text{eff}}(z) dz, \quad (6)$$

and repeat the aforementioned simulation to compute $P(\text{galaxy counts} > 1|\text{DM}_{\text{exgal}})$. The results from this simulation are shown in Supplementary Fig. 4c. We find that the probability of existence of more than one galaxy within 6" of the localization is $\lesssim 3.48^{+0.18\%}_{-0.19\%}$, again quantifying the rarity of this scenario.

Hostless DSA FRBs

We quantify the likelihood of the possibility that some of the 12 hostless DSA FRBs, which were not associated with hosts down to an r-band magnitude of $\lesssim 23.5$ mag, could actually have hosts within the local universe, specifically in the redshift bin $z \leq 0.2$. To investigate this, we use the extragalactic DMs of these FRBs to quantify how rare the excess local DM_{host} would need to be for a sufficient number of $z \leq 0.2$ hosts to exist in this sample of hostless FRBs to break our low-mass hosts deficit statistics.

Following our companion paper¹⁴, we assume a log-normal distribution for the host contribution to the DM with parameters $\mu_{\text{host}} = 4.8$ and $\sigma_{\text{host}} = 0.5$ (shown in Supplementary Fig. 5). We compute the P -values for each FRB as the probability $P(\text{DM}_{\text{host}} > \text{DM}_{\text{exgal}} - \langle \text{DM}_{\text{IGM}}(z=0.2) \rangle)$. We subtract the median DM contribution from the IGM at $z = 0.2$ of $\text{DM}_{\text{IGM}} = 180 \text{ pc cm}^{-3}$. Under the hypothesis that some of these 12 FRBs may exist at $z \leq 0.2$, these DM_{host} values would represent the extreme scenario. This is because, if these FRBs were at $z < 0.2$, then DM_{IGM} would be lower and the corresponding DM_{host} would be larger, thus pushing to the tail of the DM_{host} distribution, making the scenario of the FRB existing at lower redshifts even rarer.

Because about 20% of the star formation in the Universe at $z \leq 0.2$ occurs in low-mass galaxies ($\log M_* \leq 9$) and the FRB sample has a total of 20 FRBs with $\log M_* \geq 9$ at $z \leq 0.2$, we require five low-mass, low-redshift hosts in the hostless sample for FRBs to perfectly trace star formation in the Universe and to break our low-mass hosts deficit statistics. We therefore compute the probability that 5 of 12 hostless FRBs are low-mass, low-redshift hosts as the sum of the product of P -values of all possible combinations of five FRBs out of the 12 hostless candidates. We find that the probability of this scenario is about 10^{-7} (5.3 σ significance), implying that the probability of five of these 12 hostless FRBs being part of our local-universe sample is low. We note that this analysis assumed nothing about the host association procedures. Therefore, our analysis supports the conclusion that the deficit of low-mass hosts among the DSA-discovered FRBs is not because of observational or association limitations but reflects a genuine lack of such hosts in our sample.

Optical/infrared imaging and spectroscopy

Given the outlined selection criteria, we make use of a range of high-quality archival optical to NIR imaging data for most of the host galaxies in our sample, obtained from surveys such as PS1, BASS, MzLS²⁵, SDSS²⁶, 2MASS²⁷ and WISE²⁸. Furthermore, we incorporate near-ultraviolet and far-ultraviolet photometry from the GALEX²⁹ survey whenever available. For most of our FRB host galaxies, we use archival photometry from the respective published catalogues of these surveys, except for BASS, MzLS and SDSS. Specifically, for WISE data, we use the aperture 2 instrumental photometry to accurately capture the flux solely from the host galaxy, thereby avoiding contamination from other sources and accounting for the change in point spread function with wavelength⁴. We convert the photometry of 2MASS and WISE catalogues from Vega to AB magnitudes. We execute photometry on SDSS, BASS and MzLS imaging by iteratively fitting elliptical isophotes to the BASS r-band images of the galaxy using standard procedures

defined in photutils⁶⁷ to identify the isophote that captures $\gtrsim 95\%$ of the light from the galaxy and then convolving this aperture with the point spread function of all images to measure the instrumental magnitudes in all bands. These instrumental magnitudes were subsequently calibrated using the standard zero point of 22.5 for SDSS, BASS and MzLS. For FRB host galaxies exhibiting extended spiral/disk-like features, we perform manual photometry on all optical imaging by using isophotal analysis and consistent apertures across all bands, as described above. For PS1, we use zero points from the headers. The data for FRB 20220509G is contaminated by the presence of a star in its vicinity. We use the procedures from its discovery paper to remove the star⁴⁶ before performing photometry.

To enhance the marginal detections in the PS1, BASS or MzLS surveys, we acquire deeper optical imaging in the SDSS g', r', i' and z' bands using the WaSP¹⁷ instrument mounted on the Palomar 200-inch Hale Telescope. We complement optical data with NIR data in J, H and K_s bands obtained with the WIRC¹⁸ instrument, also mounted on the Palomar 200-inch Hale Telescope. The WaSP data are obtained as a set of six 300-s exposures in all bands. For WIRC data acquisition, we use nine-point dither patterns with appropriate exposure times and coaddition strategies: 45-s exposures with one coadd for the J band, 6-s exposures with five coadds for the H band and 3-s exposures with ten coadds for the K_s band. We calibrate the images by applying bias correction and flat-fielding, followed by cosmic rays removal using the Astro-SCRAPPY package⁷². We extract all point sources in the image using SExtractor and obtain an astrometry solution by a cross-match with the Gaia Data Release 2 catalogue⁷³. We then resample all images on the same astrometric grid to align their position angles using SWarp⁷⁴ and median-combine them to obtain stacked images. We use SExtractor to extract all $\geq 2\sigma$ sources in the stacked images and calibrate the source magnitudes by correcting for zero points computed by cross-matching SExtractor-identified sources with the # II/349/ps1 catalogue for the WaSP and the 2MASS catalogue for the WIRC. Furthermore, to ensure consistency across different photometric systems, we converted the Vega magnitudes of WIRC imaging to the AB magnitude system. Finally, we correct for interstellar dust reddening and galactic extinction along the line of sight^{75,76}. All of the imaging and photometry used in our work are catalogued in Supplementary Table 3.

Apart from the fundamental insights garnered through photometry alone, the spectrum of the host galaxy serves as an indispensable reservoir of information crucial for constraining its SFH. To this end, we obtain optical spectroscopy of FRB host galaxies. The observations were taken with the LRIS²⁰ on Keck I, DEIMOS²¹ on Keck II at the W. M. Keck Observatory and the Double Spectrograph²² on the 200-inch Hale Telescope at Palomar Observatory. The facilities, instruments, configurations and observation details for each FRB host are listed in Supplementary Table 2. The LRIS, DEIMOS and DBSP data were reduced using the LPipe⁷⁷, the Python Spectroscopic Data Reduction Pipeline (Pypelt)^{78,79} and the DBSP_DRP⁸⁰ software. All of the spectra are flux calibrated using observations of standard stars. We measure the spectroscopic redshift and emission-line fluxes of the host galaxies using the pPXF software^{23,81}. We jointly fit the stellar continuum and nebular emission using the MILES stellar library⁸². The reduced spectra with pPXF fits in the rest frame of hosts are shown in Supplementary Fig. 7. We fit the stellar-continuum-subtracted emission lines with Gaussian profiles to measure line fluxes.

Stellar population modelling

We forward model our photometry and spectroscopy data to derive the posterior parameter distribution of our host galaxies under the statistical inference framework offered by the Prospector software²⁴. The model parameters describe the stellar, nebular, AGN and dust components of the galaxy, along with instrument parameters, and we specify the noise model and priors. For Bayesian forward modelling, Prospector uses the Flexible Stellar Population Synthesis (Python-FSPS)^{83,84} code

to compute the emergent galaxy spectrum by combining simple stellar populations, given a set of stellar population parameters. We sample the posteriors using the dynamic nested sampling routine *dynesty*⁸⁵.

We use a non-parametric model that consists of a piece-wise constant SFH, for which the ratio of the average SFR in each lookback time bin is used to parameterize the stellar mass formed in that bin. This approach offers more flexibility in modelling the unusual shapes of SFHs that are not captured by parametric forms, thus reducing any biases that may exist from the strong prior of a particular parametric form of the SFH. Non-parametric models have been shown to be better suited to recover the shape of recent and older SFHs²⁴. This is important in inferring the stellar masses, mass-weighted stellar ages, recent SFRs and delays from star-formation events. Hence, we choose to use non-parametric models in our work. We use a continuity non-parametric SFH with seven bins and use the recommended StudentT prior on the SFR ratios. The SFRs in the two most recent bins (0–30 Myr and 30–100 Myr) are expected to be constrained by the nebular emission-line features in the spectrum, the ultraviolet photometry and the infrared photometry (through dust emission), if available. The remaining five bins are spaced logarithmically uniform in time up to the age of the Universe at the redshift of the galaxy.

For SED modelling, we assume the Kroupa initial mass function⁸⁶. Because a reliable measurement of stellar metallicity in the absence of high-quality absorption features in the spectrum can be difficult, we enforce the mass–metallicity relation of galaxies⁸ in our model. This prior also helps in breaking the age–metallicity degeneracy. We include the effects of dust attenuation as a dust screen affecting stars of all ages, in which the normalization of the wavelength dependence of the optical depth⁸⁷ at 5,500 Å, the extra attenuation towards young stars and the offset in slope from the dust attenuation curve⁸⁸ are the free parameters. We also use the three-component dust emission model⁸⁹ provided in FSPS, in which only the component describing the grain size distribution through the fraction of grain mass in polycyclic aromatic hydrocarbons is left as a free parameter. Because this grain model produces dust emission above 1 μm, we include it in our models only when data at these rest-frame wavelengths are available. Owing to substantial mid-infrared emission and important implications of dust-obscured AGN on the stellar ages and SFRs, we also include an AGN dust torus emission component⁹⁰ in our models whenever mid-infrared data are available. The inclusion of AGN templates smoothes out the derived SFH by removing the misidentified dust emission around asymptotic giant branch stars in the 0.1–1-Gyr lookback time bins⁹¹. Because we are jointly fitting photometry and spectroscopy with abundant emission-line features, we also include a nebular emission model. We tie the gas-phase metallicity to the stellar metallicity and float the nebular ionization parameter. The nebular emission model in Prospector assumes that all of the emission lines are powered by young stars, which may not be true in the presence of hard ionizing fields of AGNs or shock-heated emission. Hence, we marginalize over the amplitude of emission lines in our observed spectrum. We initialize the redshift to the value obtained from pPXF fits with a uniform prior width of 1% to allow for a better fit to emission and absorption lines.

Owing to systematics in measuring photometry and uncertainties in the underlying stellar and photoionization models, we assume further 10% photometric errors as done in previous works²⁴. To avoid corrupting normalization-sensitive parameters by gross aperture corrections, we scale the spectrum to match the integrated photometry examined by the population and fit for a 12th-order Chebyshev polynomial as a multiplicative calibration function. We include spectral smoothing to account for the line-of-sight velocity distribution of stars and the instrumental resolution to better fit the emission lines and incorporate a pixel outlier model to marginalize over poorly modelled noise. We apply further masking in the noisy parts of the spectrum.

All of the fixed and free parameters in our SED models with their priors are summarized in Supplementary Table 4. Supplementary

Fig. 8 shows the SED fits for all FRBs included in our sample and the key derived properties from our analysis are listed in Supplementary Table 6, in which we report the median and 68% credible intervals. By default, Prospector computes the formed stellar mass and we compute the current stellar mass by multiplying it with the surviving mass fraction, which takes into account mass loss during evolution from stellar winds and supernovae. We convert the optical depth towards young and old stellar light to V-band attenuation in magnitudes by multiplying by 1.086. We compute the average SFR over the recent 20 and 100 Myr using our constrained non-parametric SFH. We compute the rest-frame r-band absolute magnitude, $(g-r)^0$ colour and $(u-r)^0$ colour using posterior distributions of modelled SEDs.

Comparison samples and ensemble statistics

We construct several comparison sets to place FRB host galaxies within the broader context of the background galaxy population and to compare them with various transient classes. In this section, we summarize all comparison sets and the observational biases inherent in their selection. Further, we also discuss the statistical techniques used to compare the distributions of their properties.

Background galaxy population. With the ultimate goal of avoiding any systematics from the differences in stellar population modelling techniques for our FRBs and the background galaxy population, we use galaxy population data products presented in refs. 33,34 to simulate a complete population of background galaxies. These data products were derived using the properties of galaxies in the COSMOS-2015 (ref. 92) and 3D-HST⁹³ galaxy catalogues, inferred using similar Prospector-based procedures as ours, including a seven-component SFH, a two-component flexible dust attenuation model, nebular emission and AGN-heated dust-torus emission^{33,34,94}. The 3D-HST photometric catalogue comprises approximately 23,000 galaxies from roughly 900 arcmin² field of view at redshifts $z \in [0.5, 1]$ with rest-frame photometry in the range 0.3–8.0 μm and spectroscopic/grism redshifts for 30% of the objects. The COSMOS-2015 photometric catalogue comprises approximately 48,500 galaxies from 2 deg² COSMOS field at redshifts $z \in [0.005, 0.8]$ with photometry covering rest frame 0.2–24 μm and photometric redshifts for most objects.

We first summarize the reasons for not directly using the COSMOS-2015 and 3D-HST galaxy catalogues as our comparison sample. First, because the massive galaxies in the Universe are rare and the field surveyed is on the order of a degree squared, the volume investigated at low redshifts is insufficient to find enough massive galaxies. This would lead to limited-number statistics at the high-mass end of the background galaxy population, thus preventing any meaningful comparisons. Furthermore, both of these surveys are luminosity-limited. Consequently, the 3D-HST survey is complete down to about $10^{8.7} M_{\odot}$ at a redshift of $z = 0.65$ and the COSMOS-2015 survey is complete down to about $10^{8.6} M_{\odot}$ at a redshift of $z = 0.175$ and about $10^{9.1} M_{\odot}$ at a redshift of $z = 0.5$ (ref. 33). This mass-incompleteness for low-mass galaxies would imply that they are substantially under-represented in these galaxy catalogues, thus again preventing any meaningful comparisons.

To address these limitations, we take steps to compensate for incompleteness in data by simulating a representative sample of the background galaxy population. This involves using established models for the stellar mass function³³, SFMS³⁴ and star-formation density³⁴ within ranges for which existing catalogues are complete in stellar mass and SFR. Because the models presented in refs. 33,34 are for redshifts $z > 0.2$, we extend them reasonably to encompass lower redshifts ($z \leq 0.2$). In the following, we present our methodology of generating the background galaxy population in detail to enable readers to reproduce our results. We also make our script publicly available at https://github.com/krittisharma/frb_host_sharma2024.

To generate a population of N background galaxies at a given redshift z , we first sample N stellar masses in the range $\log M_* \in [7, 12]$ from the

Article

stellar mass function constructed using the continuity model fits for the redshift evolution³³. Leja et al.³³ parameterized the redshift evolution of the galaxy stellar mass function, $\Phi(\mathcal{M}, z)$, as a sum of two Schechter functions, such that a single Schechter function is written as

$$\Phi(\mathcal{M}) = \ln(10) \phi_* 10^{(\mathcal{M}-\mathcal{M}_*)(\alpha+1)} \exp(10^{(\mathcal{M}-\mathcal{M}_*)}), \quad (7)$$

for a given ϕ_* , $\mathcal{M}_* = \log M_*$ and α . For the sum of two Schechter functions, there are a total of five parameters: ϕ_1 , ϕ_2 , \mathcal{M}_* , α_1 and α_2 . The redshift evolution of ϕ_1 , ϕ_2 and \mathcal{M}_* is modelled with a quadratic equation in redshift as

$$\rho_i(z) = \lambda_{i,0} + \lambda_{i,1}z + \lambda_{i,2}z^2, \quad (8)$$

in which $\lambda_{i,j}$ are the continuity model parameters and α_1 and α_2 are assumed to be independent of redshift to limit degenerate solutions. We refer the reader to ref. 33 for the values of these parameters in the continuity models (listed in Fig. 3 of that paper). Although ref. 33 presents model fits in the mass completeness regime for redshifts $z > 0.2$, the parametric representation of the models facilitate extrapolation to lower stellar masses and lower redshifts.

After sampling N galaxy stellar masses from the mass function at redshift z , we determine the SFR for each stellar mass by referencing the density distribution of galaxies $\rho(\log M_*, \log \text{SFR}, z)$. This density distribution has been modelled using normalizing flows in ref. 34, which provides an uncertainty-deconvolved distribution of galaxies in the SFR– $\log M_*$ plane at a fixed redshift z . We refer the readers to ref. 34 for details of the normalizing flows neural network. We use the trained model publicly available at https://github.com/jrleja/sfs_leja_trained_flow. Therefore, for each galaxy stellar mass $\log M_*$ at redshift z , we sample a SFR from the probability distribution $\rho(\log \text{SFR} | \log M_*, z)$ in the range $\log \text{SFR} \in [-5, 3]$.

In the following, we discuss how we sample a SFR in the instances in which either the stellar mass falls below mass-completeness thresholds or the redshift is $z \leq 0.2$. Because our methodology for the same involves using the location of the centre of the SFMS, we first elaborate on it. Reference 34 parameterizes the galaxy SFMS as

$$\log(\text{SFR}) = \begin{cases} a(\log M - \log M_t) + c, & \log M > \log M_t \\ b(\log M - \log M_t) + c, & \log M \leq \log M_t \end{cases} \quad (9)$$

in which a is the slope at high masses, b is the slope at low masses, c is the intercept and $\log M_t$ is the stellar mass at which the slope transitions from the low-mass component to the high-mass component. The redshift evolution of these parameters is modelled using equation (8). We refer the reader to ref. 34 for the values of these parameters (listed in their Table 1).

At a particular redshift (z), when the stellar mass ($\log M_*$) falls below the completeness threshold ($\log M_{\text{comp}}$), for SFR in the range $\log \text{SFR} \in [-5, 3]$, we first compute the probability distribution of SFRs at the completeness threshold, $P(\log \text{SFR}) = \rho(\log \text{SFR} | \log M_{\text{comp}}, z)$ and the offset between the centre of the SFMS at M_{comp} and M_* , which we denote as $\Delta_{\text{SFMS}}(z, M_{\text{comp}} \rightarrow M_*)$. We then sample a SFR from the probability distribution adjusted to match the corresponding centre of the SFMS at $\log M_*$ as $P_{\Delta}(\log \text{SFR}) = P(\log \text{SFR} + \Delta_{\text{SFMS}}(z, M_{\text{comp}} \rightarrow M_*))$.

Because the centre of the SFMS is parametrically formulated for redshift evolution, we can confidently extrapolate the galaxy models to low redshifts, as detailed below. To compute a SFR corresponding to stellar mass $\log M_*$ at a particular redshift $z \leq 0.2$, we first compute the probability distribution of SFRs for stellar mass $\log M_*$ at $z' = 0.25$, $P(\log \text{SFR}) = \rho(\log \text{SFR} | \log M_*, z')$ and the offset between the centre of the SFMS for $\log M_*$ at z and z' , which we denote as $\Delta_{\text{SFMS}}(z' \rightarrow z, M_*)$. We then sample a SFR from the probability distribution adjusted to match the corresponding centre of the SFMS at z as $P_{\Delta}(\log \text{SFR}) = P(\log \text{SFR} + \Delta_{\text{SFMS}}(z' \rightarrow z, M_*))$.

Next, we quantify the uncertainty from the extrapolation into the low-mass regime and into the low-redshift regime. Note that the population model already includes the effect of cosmic variance on the high-mass regime, which is small because we assume a smooth redshift evolution, which mitigates cosmic variance, and COSMOS is a wide-area survey. We perform a simple calculation of these uncertainties by testing two extreme scenarios: (1) for the low-redshift extrapolation, we test the (close to the worst case) scenario in which there is no redshift evolution; (2) for the low-mass extrapolation, we test the (close to the worst case) scenario in which the power-law index has further 10% uncertainty when the extrapolation begins. We include a few sanity checks of these tests in Supplementary Fig. 10 for reference. Note that the evolution of mass function from $z = 0.2$ to $z = 0$ is $\lesssim 0.1$ dex (see Supplementary Fig. 10a) and the extra 10% uncertainties on the low-mass end leads to a relatively higher number of low-mass galaxies with higher SFRs (see Supplementary Fig. 10b,c). The results from our tests of these two extreme worst-case scenarios are shown in Supplementary Fig. 11 and we discuss these in detail below.

In the first test (extreme scenario 1), we find that the curve of the stellar-mass-weighted background distribution changes negligibly, which is primarily because the change in galaxy stellar mass function from redshift $z = 0.2$ to $z = 0$ is small (see Supplementary Fig. 10a). The SFR-weighted background distribution shifts by about 0.1 dex. These shifts lead to a P -value of < 0.001 against the mass-weighted distribution and 0.049 against the SFR-weighted distribution. In the second test (extreme scenario 2), as expected, we find that the stellar-mass-weighted distribution does not change because, for extra errors in the power-law index of the galaxy main sequence, only SFRs are affected and the stellar-mass-weighted stellar mass distribution remains the same. We find that the SFR-weighted distribution shifts by < 0.1 dex at the low-mass end. This is primarily because a higher uncertainty on the power-law index of the galaxy SFMS results in relatively more low-mass galaxies with higher SFRs (see Supplementary Fig. 10b,c). Because the shifts in the SFR-weighted curve is $\lesssim 0.1$ dex in both cases, the uncertainties from these extreme and worst-case scenarios are small, thus quantifying the effects of extrapolation. This implies that our results are not affected by the extra uncertainties from the extrapolation.

Finally, we adjust this simulated background population to account for optical selection effects in our sample of FRB host galaxies. We retain only those galaxies with r-band magnitudes ≤ 23.5 . To convert stellar mass to r-band magnitudes, we use estimates for mass-to-light ratios from the COSMOS-2015 and 3D-HST galaxy catalogues, accounting for variations in the mass-to-light ratios distributions across different redshift ranges. Specifically, we use $\log(M/L) \sim \mathcal{N}(0, \sigma)$, in which $\sigma = 0.2$ for $z \in [0, 0.2]$, $\sigma = 0.26$ for $z \in [0.2, 0.4]$ and $\sigma = 0.3$ for $z \in [0.4, 0.7]$.

FRB host galaxies. For comparing the stellar population properties of the host galaxies, together with our 26 secure host associations, we include the refined host properties of 23 FRBs reported in ref. 4 of previously published FRBs^{95–97} discovered by Commensal Real-Time ASKAP Fast Transients (CRAFT)⁹⁸ survey on the Australian Square Kilometre Array Pathfinder (ASKAP)⁹⁹, the More TRansients and Pulsars (MeerTRAP)¹⁰⁰ project on the MeerKAT radio telescope¹⁰¹, the Canadian Hydrogen Intensity Mapping Experiment (CHIME)¹⁰², Arecibo^{103,104} and Parkes¹⁰⁵. The selection criterion of the sample in ref. 4 particularly excluded FRB 20190614D and FRB 20190523A owing to their low PATH association probabilities. Furthermore, the investigators of that study also exclude FRB 20200120E and the galactic source SGR J1935+2154 because of their low burst spectral energies. We also include the four recently reported host galaxies of non-repeating FRBs discovered by CHIME in the local volume with low extragalactic DMs and high galactic latitudes⁵. All of these host galaxies have been modelled using similar techniques as we use in this work, thus avoiding any

modelling biases within the FRB host galaxies sample. Therefore, our FRB host galaxies properties sample consists of five repeaters and 47 apparent non-repeaters. For constructing the FRB offset distribution, together with our 26 secure host associations, we use published FRB offset measurements^{106,107}. Reference 106 used high-resolution Hubble Space Telescope ultraviolet and infrared imaging to study the host galaxy morphology and quantify the galactocentric offsets of ten FRBs. Reference 107 expanded this sample of FRB galactocentric offsets with adaptive-optics-aided diffraction-limited NIR imaging of four new FRB host galaxies.

FRBs in low-mass galaxies. Our selection criterion of r-band magnitude $\lesssim 23.5$ mag excludes one low-mass ($M_* \lesssim 10^9 M_\odot$) host (FRB 20121102A) from the sample. There is a dearth of low-mass FRB hosts at $z < 0.2$, despite a lack of expected radio selection bias for FRBs in low-mass, low-redshift galaxies. The mean $H\alpha$ luminosity of low-mass galaxies is about 10^2 times smaller than higher-mass star-forming galaxies¹⁰⁸, suggesting that the DM contributions of these galaxies' ISMs should be correspondingly small³⁶. On the basis of the DM and scattering of pulsars in the Magellanic Clouds, Ocker et al.³⁶ predict typical DMs $\lesssim 100$ pc cm⁻³ and scattering timescales < 1 ms at 1 GHz from the ISMs of low-mass galaxies, well within the selection constraints of the DSA-110 and all other FRB surveys.

An alternative selection bias against finding FRBs in low-mass galaxies could be induced if circumsource environments of FRBs in low-mass galaxies are systematically more extreme. A handful of FRBs have been localized to low-mass galaxies with elevated host DM^{109–111}, which necessitates a dense compact region near the source to account for the entirety of the DM excess. This is unlike typical FRBs in our sample¹⁴ and challenges the notion that these FRBs are similar to the broader FRB population, thus highlighting their distinctiveness³⁶.

Host galaxies of other transients. We compile the CCSNe host galaxy sample from ref. 37, which consists of 831 spectroscopically classified CCSNe discovered by the Palomar Transient Factory (PTF) in a blind search with a median redshift of $z = 0.04$ (1σ interquartile range 0.02–0.08). In the construction of this sample, the authors excluded 12 transients with uncertain CCSNe spectroscopic classifications and five hostless CCSNe with $< 2\sigma$ detections in archival data and rest-frame R-band luminosities $M_R \gtrsim -13.6$ mag, thus comprising the faintest CCSNe host galaxies discovered by the PTF. Despite these minor limitations in completeness, their study makes use of the substantial statistical power offered by their large sample size to convincingly affirm that Type II CCSNe effectively trace star formation in the Universe. The host galaxies in this sample were modelled with a τ -linear exponentially declining SFH with an average photometric coverage spanning far-ultraviolet to the mid-infrared, thus yielding fairly robust stellar mass and SFR measurements. We also retrieve the CCSNe projected galactocentric offsets reported in ref. 37 and host-normalized galactocentric offsets reported in ref. 112.

For SLSNe, we use 55 host galaxies reported in the PTF sample of ref. 37 with a median redshift of $z = 0.18$ (1σ interquartile range 0.11–0.28). This sample also excluded five hostless SLSNe between $z = 0.4$ and 1. We use the SLSNe offset measurements from Hubble Space Telescope imaging for 16 sources reported in ref. 113. We retrieve host galaxy properties for 14 IGRBs from ref. 114 and 17 IGRBs from ref. 39. Vergani et al.¹¹⁵ reported the host galaxy properties of $z < 1$ IGRBs in the BAT6 complete sample, measured using an exponentially declining SFH. The sample of Taggart and Perley³⁹ consists of all $z < 0.3$ IGRBs discovered before 2018 with an associated optical counterpart to ensure robust host associations. The host galaxies in this work were modelled using an exponentially declining SFH. The combined sample has a median redshift of $z = 0.28$ (1σ interquartile range 0.09–0.62). For offset distribution analysis, we use projected galactocentric offsets measured in ref. 115 for a complete sample

of 79 IGRBs localized by their afterglow detections. The host galaxies sample of 119 Type Ia supernovae discovered by the SNfactory reported in ref. 116 has a median redshift of $z = 0.07$ (1σ interquartile range 0.03–0.12). The investigators measure stellar mass using the magnitudes and mass-to-light ratios computed using galaxy colours. The SFR was measured using stellar population synthesis models. For constructing offset distributions, we use the measurements reported in ref. 117 for the complete sample of 113 nearby Type Ia supernovae discovered by the Carnegie Supernova Project. We use the host galaxy properties reported in ref. 118 for 31 sGRBs with robust host associations and spectroscopic redshifts with a median redshift of $z = 0.46$ (1σ interquartile range 0.20–0.78). These measurements were made by assuming a delayed- τ exponentially declining SFH. We use the corresponding galactocentric offsets presented in ref. 119. We retrieve host galaxy properties and galactocentric offsets of ULX sources from ref. 120. We specifically include only reliably classified, non-nuclear sources to avoid confusion with AGN. We further impose a minimum X-ray luminosity threshold of 10^{39} erg s⁻¹ and only include sources within a luminosity distance of 40 Mpc to avoid source confusion.

Comparison methods. Because the redshift distribution of different classes of transients is notably different, we correct their measured host galaxy stellar mass and SFR for redshift evolution¹²¹. To ensure that the statistical properties of each transient are representative of galaxies at redshift zero, for a transient host galaxy with stellar mass $M_*^{z=z_t}$ at $z = z_t$, we first compute the equivalent stellar mass, $M_*^{z=0}$, at redshift $z = 0$ such that the fraction of total star formation in the Universe below that stellar mass remains the same:

$$\frac{\int_0^{M_*^{z=0}} \Phi(M_*, z=0) \text{SFR}(M_*, z=0) dM_*}{\int_0^\infty \Phi(M_*, z=0) \text{SFR}(M_*, z=0) dM_*} = \frac{\int_0^{M_*^{z=z_t}} \Phi(M_*, z=z_t) \text{SFR}(M_*, z=z_t) dM_*}{\int_0^\infty \Phi(M_*, z=z_t) \text{SFR}(M_*, z=z_t) dM_*}. \quad (10)$$

Because the evolution in the log-normal distribution of galaxies about the SFMS is negligible over the redshift range of interest¹²², we measure the offset of the host galaxy from the SFMS at the redshift of the transient and then compute the equivalent SFR at $z = 0$ using this offset and $M_*^{z=0}$. Having corrected the galaxy properties for redshift evolution, we then perform Monte Carlo simulations to compare distributions of FRB properties with other galaxy samples. We generate 1,000 samples for the measured property of each transient, assuming a normal distribution centred at the median value with a width of reported 1σ asymmetric errors. We then perform two-sample KS tests to compute the P -value to test the null hypothesis that the two distributions are drawn from the same parent distribution. We repeat this evaluation for all 1,000 Monte Carlo simulations and report the median P -value.

We note that these corrections for redshift evolution depend on several assumptions. Therefore, we complement the KS test P -values with an independent test statistic to compare different classes of transients without the need for redshift correction. For each event E_i^j of a particular transient class i , at redshift z_i^j , we simulate 10,000 background galaxies at the same redshift as the transient. We then compute the fraction of the background population at that redshift with the property q (say, stellar mass or SFR) less than the property of our transient, denoted as $f_{i,q}^j$. Having computed how extreme the locations of these events are with respect to the background galaxy population at their redshifts, we define the test statistic as:

$$TS_q = - \sum_{j=0}^{N_i} \log f_{i,q}^j \quad (11)$$

Article

in which N_i is the number of events in transient class i . The closer the values of this test statistic to the transient under consideration, the higher the similarity between them. We compute these test statistics for 1,000 Monte Carlo simulations for each transient event, assuming a normal distribution centred at the median value with asymmetric 1σ errors, and report the median values of the test statistic.

Dominant ionization mechanism

The measured nebular emission-line fluxes can be used to identify the principal excitation mechanism in the galaxies, such as HII regions (photoionization by O- and B-type stars), planetary nebulae (photoionization by stars much hotter than O-type stars), photoionization by a power-law continuum (Seyfert galaxies) and excitation by shock-wave heating (LINER galaxies). This analysis is an important check for the validity of the SED modelling framework described above, which, for example, assumes that an active galactic nucleus does not dominate the optical light of a galaxy. The classic Baldwin, Phillips and Terlevich (BPT) empirical optical emission-line diagnostic diagrams use the $H\beta/\lambda4861$, $[OIII]\lambda5007$, $H\alpha/\lambda6563$, $[NII]\lambda6584$, $[SII]\lambda\lambda6717, 31$ and $[OI]\lambda6300$ emission-line fluxes to discriminate between different excitation mechanisms³⁰. We use the emission-line fluxes measured from stellar-continuum-subtracted spectra to determine the dominant source of ionization in FRB host galaxies. For host galaxies that lack spectral coverage, we use the emission-line measurements as predicted by our best posterior SED fit. We use the theoretical maximum starburst line¹²³, the pure star-forming galaxies versus Seyfert-H II composite objects classification line¹²⁴ and the Seyfert versus LINER classification lines³¹ to classify our FRB host galaxies into star-forming, composites, Seyferts and LINERs. The emission-line ratios and the classification lines are plotted in Extended Data Fig. 2. We also plot the local emission-line galaxies with S/N ratio ≥ 10 from the SDSS for ref. 26. We note a systematic offset between the star-forming locus and DSA FRBs in Extended Data Fig. 2a. This may be because of leakage of $H\alpha$ flux to $[NII]$. We believe so because with the other two emission-line ratio metrics (see Extended Data Fig. 2b,c), the DSA FRBs are indeed consistent with the locus of star-forming background galaxies.

The host galaxies of FRB 20220509G, FRB 20221101B and FRB 20221012A are classified as LINER galaxies, whereas those of FRB 20230307A and FRB 20221116A are classified as Seyfert galaxies. The host galaxy of FRB 20221116A is a massive star-forming spiral galaxy at its redshift, which are relatively rare. This galaxy exhibits a post-starburst SFH, with a rapid decline in its SFR over the past 100 Myr. The BPT emission-line diagnostics indicate LINER activity and the stellar mass of the galaxy suggests the presence of a supermassive black hole (SMBH) with a mass of $\log M_{BH} = 8.06 \pm 0.31$ (ref. 125). Given these characteristics, it is plausible that the SMBH is contributing to the observed quenching of star formation by means of AGN feedback mechanisms. Quenching timescales derived from IllustrisTNG simulations, which incorporate both quasar mode and radio mode AGN feedback, span a broad range from hundreds of millions of years to tens of billions of years (ref. 126). Specifically, for galaxies with a similar stellar mass and central SMBH mass, the expected quenching timescale is about 2 Gyr. This inferred timescale is potentially consistent with the observed reduction in SFR, provided the star formation continues to decline at the rate observed over the past 100 Myr. Thus, although SMBHs are not the sole mechanism for quenching in galaxies, the evidence from both observational diagnostics and simulations supports the hypothesis that AGN feedback may be a notable contributor to the quenching observed in the host galaxy of FRB 20221116A. The τ -linear exponentially declining SFHs of the host galaxies of FRB 20220509G, FRB 20221012A and FRB 20230307A with low specific SFRs and substantial f_{AGN} estimated by our SED analysis also support the presence of an AGN component in these galaxies. Most FRB hosts align with the star-forming locus of background galaxies, reflecting their high degree of star formation revealed by SED analysis. This is consistent

with the results of refs. 95, 97, 127. We statistically quantify these results by performing two-sample two-dimensional KS tests, in which we test the null hypothesis that, for a given ionization mechanism, both the FRBs and the background SDSS galaxy population are drawn from the same underlying population. The results from these tests are summarized in Supplementary Table 5. Using the same classification scheme for both FRB hosts and background galaxies and comparing FRB hosts with the entire galaxy population, we find that the P -value (P_{KS}) exceeds 0.05 for all three classification schemes. This suggests that we cannot statistically rule out the possibility that FRB host galaxies are consistent with the background population of emission-line galaxies. Furthermore, FRB host galaxies markedly differ from sub-populations of AGNs (LINERs and Seyferts) with a confidence level exceeding 6σ . However, they are statistically consistent with an underlying population of star-forming + LINER (consistent with the results in ref. 127) and star-forming + Seyfert galaxies ($P_{KS} \gtrsim 0.05$) across most classification schemes.

WISE colour–colour galaxy classification

The median redshift of FRBs is $z = 0.28$. At such high redshifts, it is difficult to obtain robust morphological classifications with archival ground-based optical imaging data. Indeed, we detect spiral arm features for host galaxies of only six events: FRB 20220319D, FRB 20231120A, FRB 20220207C, FRB 20231123B, FRB 20221116A and FRB 20230501A (see Fig. 1). Hence, we use the WISE colour–colour classification³² to obtain tentative galaxy classifications (see Extended Data Fig. 3). We overlay the available WISE data for 22 FRB host galaxies. The stars and early-type galaxies have $W1-W2$ colour close to zero, whereas the spiral galaxies are red in $W2-W3$ and ultraluminous infrared galaxies tend to be red in both colours. The WISE colour–colour galaxy classifications of FRB hosts are broadly consistent with BPT classifications. Most FRB host galaxies that were classified as spiral galaxies or luminous infrared galaxies in WISE colour–colour galaxy classification are also classified as star-forming or HII regions–AGN composites in the BPT diagram. Most FRB host galaxies in our sample are consistent with the locus of spiral galaxies. The only candidate elliptical galaxy is the host of FRB 20221012A, which has a τ -linear exponentially declining SFH with a low specific SFR of $0.001^{+0.001}_{-0.001}$ Gyr⁻¹, quiescent classification as per its low degree of star formation and is a composite/LINER according to BPT classifications. There are hints for AGN activity in five FRBs from our sample: FRB 20220825A (LINER), FRB 20230712A (starburst/LINER), FRB 20220307B (Seyfert), FRB 20220506D (Seyfert) and FRB 20221116A ($W1-W2 \approx 0.5$). These classifications are consistent with their BPT diagnostics, in which FRB 20220825A, FRB 20230712A, FRB 20220307B and FRB 20220506D were classified as AGN–H II regions composites and FRB 20221116A was classified as a borderline case of composites and Seyferts.

Stellar population properties

We compare the inferred host characteristics of repeaters and non-repeaters. The comparison between repeaters, non-repeaters, all FRBs and the background galaxy population of their derived galaxy properties, such as the stellar mass ($\log M_*$), SFR averaged over the recent 100 Myr ($\log SFR_{100\text{Myr}}$), specific SFR (sSFR), mass-weighted age (t_m), stellar metallicity ($\log Z/Z_\odot$) and dust attenuation of old stellar light ($A_{V,\text{old}}$), is shown in Extended Data Fig. 4. These distributions were constructed using 1,000 samples of the posterior distributions for each galaxy. The median stellar mass of the host galaxies of repeaters is $\log M_* = 9.64$ (1σ interquartile range 9.07 to 10.18), whereas for non-repeaters, the median stellar mass is $\log M_* = 10.20$ (1σ interquartile range 9.48 to 10.93). We observe that the host galaxies of repeaters are relatively less massive than that of non-repeaters. As a consequence of the mass–metallicity prior in our SED modelling, the metallicity of the host galaxies of repeaters ($\log Z/Z_\odot = -1.16$, 1σ interquartile range -1.79 to -0.58) is also lower than that of non-repeaters ($\log Z/Z_\odot = -0.45$,

1σ interquartile range –1.06 to 0.07). Because the SFR ranges examined by repeaters ($\text{SFR}_{100\text{Myr}} = 0.96 M_{\odot} \text{ year}^{-1}$, 1σ interquartile range $0.03\text{--}2.57 M_{\odot} \text{ year}^{-1}$) and non-repeaters ($\text{SFR}_{100\text{Myr}} = 1.12 M_{\odot} \text{ year}^{-1}$, 1σ interquartile range $0.84\text{--}10.90 M_{\odot} \text{ year}^{-1}$) are comparable, the sSFR of repeaters ($\text{sSFR} = 0.15 \text{ Gyr}^{-1}$, 1σ interquartile range $0.01\text{--}0.69 \text{ Gyr}^{-1}$) is higher than that of non-repeaters ($\text{sSFR} = 0.07 \text{ Gyr}^{-1}$, 1σ interquartile range $0.05\text{--}0.33 \text{ Gyr}^{-1}$). To quantify these differences, we perform a two-sample KS test between stellar population properties of the host galaxies of repeaters and non-repeaters. We find $P_{\text{KS}} \geq 0.05$ on comparing $\log M_{\star}$, SFR, sSFR, $\log Z/Z_{\odot}$, A_V and t_m . Therefore, we find no statistical evidence for differences in the host galaxy properties of repeaters and non-repeaters. These conclusions are similar to the recent results from Gordon et al.⁴, who also find no statistical difference between the hosts of repeaters and non-repeaters, as well as the observation that repeaters may exist in relatively lower-mass galaxies than non-repeaters.

Galaxy SFMS

In Extended Data Fig. 5, we show the distribution of FRB host galaxies in the $\log M_{\star}\text{--}\log \text{SFR}_{100\text{Myr}}$ space, together with the distribution of background galaxies from the 3D-HST⁹³ and COSMOS-2015 (ref. 92) catalogues in three redshift bins to minimize the effect of the SFMS evolution. The distribution of FRB host offset from the galaxy SFMS at its redshift is centred at -0.1 dex with a Gaussian scatter of 0.7 dex, which is consistent with the scatter of background galaxies about the SFMS. This observation aligns with the main findings of Gordon et al.⁴, who discovered that the host galaxies of FRBs match the characteristics of star-forming galaxies. Next, we systematically classify our host galaxies as star-forming ($D > 1/3$), transitioning ($1/20 < D < 1/3$) and quiescent ($D < 1/20$) based on their degree of star formation $D = \text{sSFR}(z) \times t_{\text{H}}(z)$, in which D is the mass-doubling number¹²⁸ and $t_{\text{H}}(z)$ is the age of the Universe at the redshift of the galaxy. Out of 30 FRB hosts published in this work, 21 are classified as star-forming, seven as transitioning and two as quiescent galaxies. Most of the observed star-forming galaxies in our sample are consistent with the notable star-forming galaxies representation in the FRB host galaxies sample of ref. 4. The quiescent state of the host galaxy of FRB 20220509G may be a consequence of it being a member of a massive galaxy cluster⁴⁶. The quiescent host galaxy of FRB 20221012A was also classified as a candidate elliptical galaxy in WISE colour–colour morphological classifications. The quiescent fraction of FRB host galaxies in the $z \leq 0.1$ and $0.1 < z \leq 0.3$ bins are $1/9$ and $2/23$, respectively, which are lower than expected for the background galaxy population in the mass range examined by FRB host galaxies³⁴.

SFHs and age of the stellar population

The SFH of the host galaxies of transients can be crucial in inferring the age of their progenitors. The timing and duration of past episodes of star formation shed light on the processes that shaped their evolution. The galaxies may exhibit different patterns of star formation over their lifetimes, ranging from intense bursts of star formation to more gradual and steady processes, which are aptly captured by non-parametric SFHs inferred from the galaxy SED fits. The constrained SFH of FRB host galaxies published in this work are shown in Supplementary Fig. 9. As most of the FRB host galaxies are $0.1\text{--}1L_{\odot}$ galaxies (see Fig. 3), it is not surprising that 50% of the FRB hosts have a delayed- τ and 16% of FRB hosts have a τ -linear exponentially declining SFH. The occurrence of FRBs in galaxies with rejuvenating (10%), post-starburst (16%) and rising (8%) SFHs adds to the diversity of possible delays from the star-formation events. The prominence of exponentially declining SFHs, with a wide variety of other SFHs, was also observed in ref. 4. This diversity underscores the complex nature of the environments in which FRBs occur and highlights the importance of understanding the detailed SFH of their host galaxies in unravelling the mysteries of FRB sources. Similar to ref. 4, we find that the distribution of FRB hosts, when compared with the background galaxy population in $\log \text{sSFR}\text{--}t_m$ space, which

are moments of the SFH, is consistent with the background population (see Extended Data Fig. 5).

Comparison with other transients

Constructing the offset distributions. We compare the offset distribution of FRBs with respect to the host-galaxy centre with different classes of transients. We compute the projected physical offsets and the corresponding host-normalized offsets using the measurements done for PATH analysis. These offsets for host galaxies in our sample, together with other transients, are plotted in Extended Data Fig. 7. Here we also include the projected offset measurements for 14 FRBs from the literature^{106,107}. We plot the errors from the 90% localization region of FRBs in which we sample 1,000 FRB locations within the localization region, while ensuring that we obtain an equal number of samples away from and closer to the centre of the galaxy to avoid any biases from the shape of the localization region. The median offset of FRB location from the centre of the host galaxies is 5.54 kpc (1.25 effective galactic radii). The results from two-sample KS tests between FRBs and different classes of transients are tabulated in Supplementary Table 7.

Constructing the galaxy properties distributions. Comparison of the stellar population properties of the host galaxies can also yield important insights on the similarity of FRBs with different transient classes^{129–131}. Because the redshift distribution of different classes of transients is substantially different, we correct their measured stellar mass and SFR for redshift evolution¹²¹. We directly compare different classes of transients in Extended Data Fig. 8 and report the results from two-sample KS tests in Supplementary Table 7. Because the conclusions from comparisons of distributions of galaxy properties corrected for redshift evolution depend on galaxy evolution assumptions, we constructed an independent test statistic to compare transients without the need for redshift correction. We also list the test statistic for all transient classes under consideration in Supplementary Table 7 and find that conclusions from these test statistics are consistent with our conclusions from KS tests performed on the redshift-corrected distribution of the host properties.

Inferring the similarities with transients. We find that, although the SFR distribution of IGRBs are consistent with FRBs ($P_{\text{KS}} > 0.05$), other host galaxy properties and offset distribution of FRBs are not consistent with SLSNe and IGRBs ($P_{\text{KS}} < 0.001$), which are concentrated in the central, star-forming regions of their low-mass host galaxies. Similar conclusions were reached by Bhandari et al.⁹⁶, who also found that FRBs occur in systematically more massive galaxies than SLSNe and IGRBs. Furthermore, refs. 96,106 also found that FRBs occur at systematically extended locations within their host galaxies, thus providing evidence that FRBs probably do not originate from sources formed by the deaths of massive stripped envelope stars. Recent work¹⁰⁷ also rejected similarities with SLSNe and IGRBs offsets with high statistical significance.

Although the projected offset and SFR distributions of ULX sources are consistent with FRBs, they occur in systematically more massive galaxies than FRBs, thus ruling out any similarities with FRBs at high statistical significance ($P_{\text{KS}} \approx 10^{-6}$). These conclusions are consistent with the previous studies⁹⁶.

Comparing with CCSNe host galaxy properties, we find that, although the SFR and sSFR distributions of CCSNe are consistent with FRBs ($P_{\text{KS}} > 0.05$), there is a deficit of low-mass galaxies, for which we ruled out similarities in stellar mass distributions with more than 95% confidence ($P_{\text{KS}} = 0.003$). Although the similarities in SFR and sSFR distributions have been observed previously in ref. 96, in contrast to those results, we find that the CCSNe host stellar mass distribution is not consistent with FRBs, with a deficit of low-mass galaxies. In the main text, we infer this low-mass host galaxy deficit as a preference of FRBs for metal-rich environments, thus supporting the scenario in which

Article

FRB sources are formed in CCSNe of stellar merger remnants, which are expected to have the requisite magnetic fields to form magnetars. Furthermore, comparing the offset distributions, we find that FRBs occur at systematically larger offsets than typical CCSNe, thus ruling out similarities with more than 95% confidence ($P_{KS} = 0.014$). This is in contrast to previous works, in which refs. 96,106,107 claim that FRB offsets are consistent with CCSNe. We infer these relatively larger offsets as FRB sources being preferentially formed in stellar mergers, which are a delayed CCSNe formation channel.

As there is no observational evidence of AIC events and binary white dwarf mergers, we assume that the offset distribution of Type Ia supernovae is representative of AIC events and binary white dwarf mergers. Owing to small natal kicks of the neutron stars formed through AIC or mergers of white dwarfs, they may not occur at such large offsets as magnetars formed as a result of binary neutron star mergers. We find that the FRB host galaxy properties and offset distribution are consistent with Type Ia supernovae ($P_{KS} > 0.05$). These results are consistent with the results from refs. 96,106,107, thus allowing for FRB sources that invoke white dwarf progenitors. Furthermore, we find that the host-normalized Type Ia supernovae offsets are systematically at lower physical offsets than our large FRBs sample. This may imply that FRBs select for a higher offset subset of Type Ia supernovae, but any differences in Type Ia supernova progenitors at large and small offsets are not characterized in the literature.

The larger offsets of FRBs compared with CCSNe and Type Ia supernovae may as well hint at different formation channels, in which larger offsets support delayed formation channels either involving kicks or when the progenitor lifetime is long enough to allow the sGRB sources to travel to the outskirts of their host galaxies¹¹⁹. Similar to in refs. 96,106,107, we find that the sGRB offset distribution is consistent with FRBs ($P_{KS} > 0.05$). However, in contrast to ref. 96, we find that, although the sGRB SFR and sSFR distributions are consistent with FRBs, the similarity of the stellar mass distribution with FRBs is ruled out at high confidence ($P_{KS} = 0.002$).

Data availability

The fast radio burst data presented here are included in the Supplementary Tables. We also publicly provide these data as a CSV file in the GitHub repository at https://github.com/krittisharma/frb_host_sharma2024.

Code availability

We have created a reproduction package for our work that includes all code used for our analysis. We have placed this code at the following GitHub link: https://github.com/krittisharma/frb_host_sharma2024.

50. Ravi, V. et al. Deep Synoptic Array science: discovery of the host galaxy of FRB 20220912A. *Astrophys. J. Lett.* **949**, L3 (2023).
51. Barsdell, B. R., Bailes, M., Barnes, D. G. & Fluke, C. J. Accelerating incoherent dedispersion. *Mon. Not. R. Astron. Soc.* **422**, 379–392 (2012).
52. CASA Team. CASA, the Common Astronomy Software Applications for radio astronomy. *Publ. Astron. Soc. Pac.* **134**, 114501 (2022).
53. Offringa, A. R. et al. WSClean: an implementation of a fast, generic wide-field imager for radio astronomy. *Mon. Not. R. Astron. Soc.* **444**, 606–619 (2014).
54. Condon, J. J. et al. The NRAO VLA Sky Survey. *Astron. J.* **115**, 1693–1716 (1998).
55. Hewitt, D. M. et al. Millisecond localization of the hyperactive repeating FRB 20220912A. *Mon. Not. R. Astron. Soc.* **529**, 1814–1826 (2024).
56. Zhang, Z. J., Yan, K., Li, C. M., Zhang, G. Q. & Wang, F. Y. Intergalactic medium dispersion measures of fast radio bursts estimated from IllustrisTNG simulation and their cosmological applications. *Astrophys. J.* **906**, 49 (2021).
57. Abbott, T. M. C. et al. The Dark Energy Survey: Data Release 1. *Astrophys. J. Suppl. Ser.* **239**, 18 (2018).
58. Ochsenbein, F., Bauer, P. & Marcout, J. The VizieR database of astronomical catalogues. *Astron. Astrophys. Suppl.* **143**, 23–32 (2000).
59. Astropy Collaboration. Astropy: a community Python package for astronomy. *Astron. Astrophys.* **558**, A33 (2013).
60. Astropy Collaboration. The Astropy Project: building an open-science project and status of the v2.0 core package. *Astron. J.* **156**, 123 (2018).
61. Tachibana, Y. & Miller, A. A. A morphological classification model to identify unresolved PanSTARRS1 sources: application in the ZTF real-time pipeline. *Publ. Astron. Soc. Pac.* **130**, 128001 (2018).
62. OMullane, W. et al. Batch is back: CasJobs, serving multi-TB data on the Web. Preprint at <https://arxiv.org/abs/cs/0502072> (2005).
63. Schlegel, D. et al. DESI Legacy Imaging Surveys Data Release 9. *Am. Astron. Soc. Meet. Abstr.* **237**, 235–03 (2021).
64. Lang, D., Hogg, D. W., Mierle, K., Blanton, M. & Roweis, S. Astrometry.net: blind astrometric calibration of arbitrary astronomical images. *Astron. J.* **139**, 1782–1800 (2010).
65. Bertin, E. in *Proc. Astronomical Data Analysis Software and Systems XX* (eds Evans, I. N., Accomazzi, A., Mink, D. J. & Rots, A. H.) 435 (Astronomical Society of the Pacific, 2011).
66. Flewelling, H. Pan-STARRS Data Release 2. *Am. Astron. Soc. Meet. Abstr.* **231**, 436.01 (2018).
67. Bradley, L. et al. astropy/photutils: 1.5.0. Zenodo <https://doi.org/10.5281/zenodo.6825092> (2022).
68. Eftekhari, T. & Berger, E. Associating fast radio bursts with their host galaxies. *Astrophys. J.* **849**, 162 (2017).
69. van der Wel, A. et al. 3D-HST+CANDELS: the evolution of the galaxy size-mass distribution since $z = 3$. *Astrophys. J.* **788**, 28 (2014).
70. Driver, S. P. et al. Measurements of extragalactic background light from the far UV to the far IR from deep ground- and space-based galaxy counts. *Astrophys. J.* **827**, 108 (2016).
71. Peebles, P. J. E. *The Large-Scale Structure of the Universe* (Princeton Univ. Press, 1980).
72. McCully, C. et al. astropy/astroscrappy: v1.0.5 Zenodo release. Zenodo <https://doi.org/10.5281/zenodo.1482019> (2018).
73. Gaia Collaboration. Gaia Data Release 2. Summary of the contents and survey properties. *Astron. Astrophys.* **616**, A1 (2018).
74. Bertin, E. et al. in *Proc. Astronomical Data Analysis Software and Systems XI* (eds Bohlander, D. A., Durand, D. & Handley, T. H.) 228 (Astronomical Society of the Pacific, 2002).
75. Green, G. dustmaps: a Python interface for maps of interstellar dust. *J. Open Source Softw.* **3**, 695 (2018).
76. Fitzpatrick, E. L. Correcting for the effects of interstellar extinction. *Publ. Astron. Soc. Pac.* **111**, 63–75 (1999).
77. Perley, D. A. Fully automated reduction of longslit spectroscopy with the Low Resolution Imaging Spectrometer at the Keck Observatory. *Publ. Astron. Soc. Pac.* **131**, 084503 (2019).
78. Prochaska, J. X. et al. pypeit/PypeIt: version 1.6.0. Zenodo <https://doi.org/10.5281/zenodo.5548381> (2021).
79. Prochaska, J. X. et al. PypeIt: the Python spectroscopic data reduction pipeline. *J. Open Source Softw.* **5**, 2308 (2020).
80. Mandigo-Stoba, M. S., Fremling, C. & Kasliwal, M. M. DBSP_DRP: a Python package for automated spectroscopic data reduction of dbsp data. *J. Open Source Softw.* **7**, 3612 (2022).
81. Cappellari, M. Improving the full spectrum fitting method: accurate convolution with Gauss–Hermite functions. *Mon. Not. R. Astron. Soc.* **466**, 798–811 (2017).
82. Sánchez-Blázquez, P. et al. Medium-resolution Isaac Newton Telescope library of empirical spectra. *Mon. Not. R. Astron. Soc.* **371**, 703–718 (2006).
83. Connroy, C., Gunn, J. E. & White, M. The propagation of uncertainties in stellar population synthesis modeling. I. The relevance of uncertain aspects of stellar evolution and the initial mass function to the derived physical properties of galaxies. *Astrophys. J.* **699**, 486–506 (2009).
84. Connroy, C. & Gunn, J. E. FSPS: Flexible Stellar Population Synthesis. *Astrophysics Source Code Library*, record ascl:1010.043 (2010).
85. Speagle, J. S. dynesty: a dynamic nested sampling package for estimating Bayesian posteriors and evidences. *Mon. Not. R. Astron. Soc.* **493**, 3132–3158 (2020).
86. Kroupa, P. On the variation of the initial mass function. *Mon. Not. R. Astron. Soc.* **322**, 231–246 (2001).
87. Kriek, M. & Connroy, C. The dust attenuation law in distant galaxies: evidence for variation with spectral type. *Astrophys. J. Lett.* **775**, L16 (2013).
88. Calzetti, D. et al. The dust content and opacity of actively star-forming galaxies. *Astrophys. J.* **533**, 682–695 (2000).
89. Draine, B. T. & Li, A. Infrared emission from interstellar dust. IV. The silicate-graphite-PAH model in the post-Spitzer era. *Astrophys. J.* **657**, 810–837 (2007).
90. Nenkova, M., Sirocky, M. M., Nikutta, R., Ivezic, Z. & Elitzur, M. AGN dusty tori. II. Observational implications of clumpiness. *Astrophys. J.* **685**, 160–180 (2008).
91. Leja, J., Johnson, B. D., Conroy, C. & van Dokkum, P. Hot dust in panchromatic SED fitting: identification of active galactic nuclei and improved galaxy properties. *Astrophys. J.* **854**, 62 (2018).
92. Laigle, C. et al. The COSMOS2015 catalog: exploring the $1 < z < 6$ Universe with half a million galaxies. *Astrophys. J. Suppl. Ser.* **224**, 24 (2016).
93. Skelton, R. E. et al. 3D-HST WFC3-selected photometric catalogs in the five CANDELS/3D-HST fields: photometry, photometric redshifts, and stellar masses. *Astrophys. J. Suppl. Ser.* **214**, 24 (2014).
94. Leja, J. et al. An older, more quiescent universe from panchromatic SED fitting of the 3D-HST survey. *Astrophys. J.* **877**, 140 (2019).
95. Bhandari, S. et al. Characterizing the fast radio burst host galaxy population and its connection to transients in the local and extragalactic universe. *Astron. J.* **163**, 69 (2022).
96. Bhandari, S. et al. The host galaxies and progenitors of fast radio bursts localized with the Australian Square Kilometre Array Pathfinder. *Astrophys. J. Lett.* **895**, L37 (2020).
97. Heintz, K. E. et al. Host galaxy properties and offset distributions of fast radio bursts: implications for their progenitors. *Astrophys. J.* **903**, 152 (2020).
98. Macquart, J.-P. et al. The Commensal Real-Time ASKAP Fast-Transients (CRAFT) Survey. *Publ. Astron. Soc. Pac.* **27**, 272–282 (2010).
99. McConnell, D. et al. The Australian Square Kilometre Array Pathfinder: performance of the Boolardy Engineering Test Array. *Publ. Astron. Soc. Pac.* **33**, e042 (2016).
100. Rajwade, K. M. et al. First discoveries and localizations of Fast Radio Bursts with MeerTRAP: real-time, commensal MeerKAT survey. *Mon. Not. R. Astron. Soc.* **514**, 1961–1974 (2022).

101. Jonas, J. & MeerKAT Team. in *Proc. MeerKAT Science: On the Pathway to the SKA*, 1 (2016).
102. CHIME/FRB Collaboration. CHIME/FRB discovery of eight new repeating fast radio burst sources. *Astrophys. J. Lett.* **885**, L24 (2019).
103. Spitler, L. G. et al. Fast radio burst discovered in the Arecibo pulsar ALFA survey. *Astrophys. J.* **790**, 101 (2014).
104. Scholz, P. et al. The repeating fast radio burst FRB 121102: multi-wavelength observations and additional bursts. *Astrophys. J.* **833**, 177 (2016).
105. Price, D. C. et al. A fast radio burst with frequency-dependent polarization detected during Breakthrough Listen observations. *Mon. Not. R. Astron. Soc.* **486**, 3636–3646 (2019).
106. Mannings, A. G. et al. A high-resolution view of fast radio burst host environments. *Astrophys. J.* **917**, 75 (2021).
107. Woodland, M. N. et al. The environments of fast radio bursts viewed using adaptive optics. *Astrophys. J.* **973**, 64 (2024).
108. Kennicutt, Jr & Robert, C. et al. An H α imaging survey of galaxies in the local 11 Mpc volume. *Astrophys. J. Suppl. Ser.* **178**, 247–279 (2008).
109. Bhandari, S. et al. A nonrepeating fast radio burst in a dwarf host galaxy. *Astrophys. J.* **948**, 67 (2023).
110. Niu, C. H. et al. A repeating fast radio burst associated with a persistent radio source. *Nature* **606**, 873–877 (2022).
111. Tendulkar, S. P. et al. The host galaxy and redshift of the repeating fast radio burst FRB 121102. *Astrophys. J. Lett.* **834**, L7 (2017).
112. Kelly, P. L. & Kirshner, R. P. Core-collapse supernovae and host galaxy stellar populations. *Astrophys. J.* **759**, 107 (2012).
113. Lunnan, R. et al. Zooming in on the progenitors of superluminous supernovae with the HST. *Astrophys. J.* **804**, 90 (2015).
114. Vergani, S. D. et al. Are long gamma-ray bursts biased tracers of star formation? Clues from the host galaxies of the Swift/BAT6 complete sample of LGRBs. I. Stellar mass at $z < 1$. *Astron. Astrophys.* **581**, A102 (2015).
115. Blanchard, P. K., Berger, E. & Fong, W.-f. The offset and host light distributions of long gamma-ray bursts: a new view from HST observations of Swift bursts. *Astrophys. J.* **817**, 144 (2016).
116. Childress, M. et al. Host galaxy properties and Hubble residuals of Type Ia supernovae from the Nearby Supernova Factory. *Astrophys. J.* **770**, 108 (2013).
117. Uddin, S. A. et al. The Carnegie Supernova Project-I: correlation between Type Ia supernovae and their host galaxies from optical to near-infrared bands. *Astrophys. J.* **901**, 143 (2020).
118. Nugent, A. E. et al. Short GRB host galaxies. II. A legacy sample of redshifts, stellar population properties, and implications for their neutron star merger origins. *Astrophys. J.* **940**, 57 (2022).
119. Fong, W.-f. et al. Short GRB host galaxies. I. Photometric and spectroscopic catalogs, host associations, and galactocentric offsets. *Astrophys. J.* **940**, 56 (2022).
120. Kovlakas, K. et al. A census of ultraluminous X-ray sources in the local Universe. *Mon. Not. R. Astron. Soc.* **498**, 4790–4810 (2020).
121. Bochenek, C. D., Ravi, V. & Dong, D. Localized fast radio bursts are consistent with magnetar progenitors formed in core-collapse supernovae. *Astrophys. J. Lett.* **907**, L31 (2021).
122. Speagle, J. S., Steinhardt, C. L., Capak, P. L. & Silverman, J. D. A highly consistent framework for the evolution of the star-forming “main sequence” from $z \sim 0$ –6. *Astrophys. J. Suppl. Ser.* **214**, 15 (2014).
123. Kewley, L. J., Dopita, M. A., Sutherland, R. S., Heisler, C. A. & Trevena, J. Theoretical modeling of starburst galaxies. *Astrophys. J.* **556**, 121–140 (2001).
124. Kauffmann, G. et al. The host galaxies of active galactic nuclei. *Mon. Not. R. Astron. Soc.* **346**, 1055–1077 (2003).
125. Greene, J. E., Strader, J. & Ho, L. C. Intermediate-mass black holes. *Annu. Rev. Astron. Astrophys.* **58**, 257–312 (2020).
126. Walters, D., Woo, J. & Ellison, S. L. Quenching time-scales in the IllustrisTNG simulation. *Mon. Not. R. Astron. Soc.* **511**, 6126–6142 (2022).
127. Eftekhari, T. et al. An X-ray census of fast radio burst host galaxies: constraints on active galactic nuclei and X-ray counterparts. *Astrophys. J.* **958**, 66 (2023).
128. Tacchella, S. et al. Fast, slow, early, late: quenching massive galaxies at $z \sim 0.8$. *Astrophys. J.* **926**, 134 (2022).
129. Beloborodov, A. M. Blast waves from magnetar flares and fast radio bursts. *Astrophys. J.* **896**, 142 (2020).
130. Margalit, B., Berger, E. & Metzger, B. D. Fast radio bursts from magnetars born in binary neutron star mergers and accretion induced collapse. *Astrophys. J.* **886**, 110 (2019).
131. Nicholl, M. et al. Empirical constraints on the origin of fast radio bursts: volumetric rates and host galaxy demographics as a test of millisecond magnetar connection. *Astrophys. J.* **843**, 84 (2017).
132. Drlica-Wagner, A. et al. Milky Way satellite census. I. The observational selection function for Milky Way satellites in DES Y3 and Pan-STARRS DR1. *Astrophys. J.* **893**, 47 (2020).
133. Harris, W. E. A catalog of parameters for globular clusters in the Milky Way. *Astron. J.* **112**, 1487 (1996).
134. Lampeit, H. et al. The effect of host galaxies on Type Ia supernovae in the SDSS-II supernova survey. *Astrophys. J.* **722**, 566–576 (2010).

Acknowledgements We thank the staff members of the Owens Valley Radio Observatory and the Caltech radio group, including K. Bernasconi, S. Cha-Ramos, S. Harnach, T. Klinefelter, L. McGraw, C. Posner, A. Rizo, M. Virgin, S. White and T. Zentmyer. Their tireless efforts were instrumental to the success of the Deep Synoptic Array (DSA-110). The DSA-110 is supported by the National Science Foundation Mid-Scale Innovations Program in Astronomical Sciences (MSIP) under grant AST-1836018. We acknowledge the use of the VLA Calibrator Manual and the Radio Fundamental Catalog. Some of the data presented here were obtained at the W. M. Keck Observatory, which is operated as a scientific partnership among the California Institute of Technology, the University of California and the National Aeronautics and Space Administration. The Observatory was made possible by the generous financial support of the W. M. Keck Foundation. K.S. thanks A. Gordon for guidance on spectral energy distribution modelling, A. Nugent and H. Kumar for valuable insights into the parallels with the short-duration gamma-ray burst host population, X. Prochaska, K. Bannister and A. Beloborodov for engaging discussions on the distribution of star formation in the Universe and the core-collapse supernova formation channel of fast radio burst sources, N. Sridhar for insightful discussions, D. Cook and J. Greene for discussions on star formation in the local universe and Y. Tomar for guidance in constructing mass functions and simulating background galaxy population.

Author contributions V.R. and G.Ha. led the development of the Deep Synoptic Array (DSA-110). D.H., M.H., J.La., P.R., S.W. and D.W. contributed to the construction of the DSA-110. K.S. and V.R. led the writing of the manuscript. K.S. developed the statistical framework to analyse the fast radio burst sample and undertook most of the optical/infrared host galaxy data analysis and interpretation. K.S., V.R., L.C., C.L., J.S., J.F., N.K., M.S., S.A., K.K.D., Y.J.Q., S.R., D.Z.D., J.M. and YY conducted the optical/infrared follow-up observations presented in this work. V.R., C.L., L.C., G.He. and R.H. developed the software pipeline for detecting fast radio bursts with the DSA-110. J.Le. and J.S. provided guidance for spectral energy distribution analysis. J.Le. provided guidance on simulating background galaxy populations.

Competing interests The authors declare no competing interests.

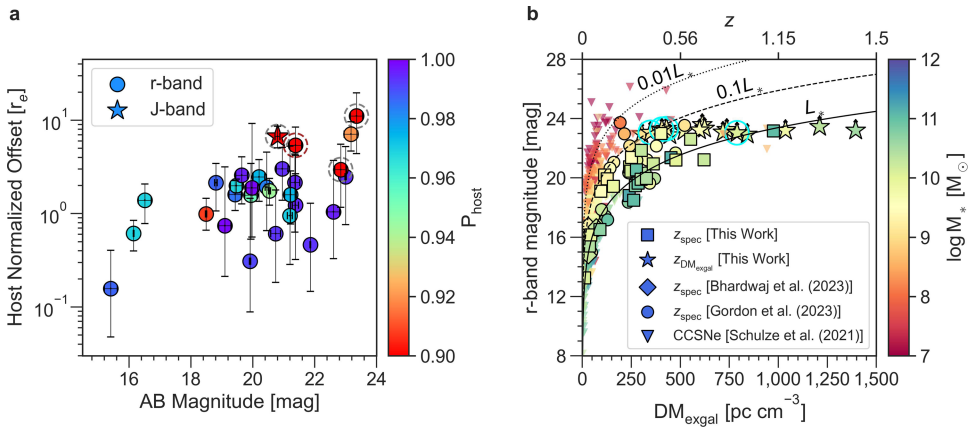
Additional information

Supplementary information The online version contains supplementary material available at <https://doi.org/10.1038/s41586-024-08074-9>.

Correspondence and requests for materials should be addressed to Kritti Sharma.

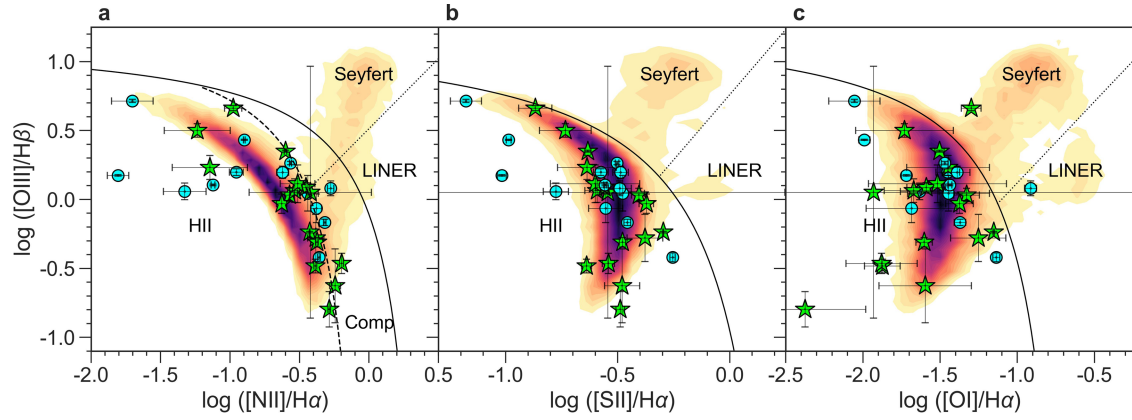
Peer review information *Nature* thanks Daniele Michilli and the other, anonymous, reviewer(s) for their contribution to the peer review of this work. Peer reviewer reports are available.

Reprints and permissions information is available at <http://www.nature.com/reprints>.


Extended Data Fig. 1 | Probabilistic host association for DSA-110-discovered

FRBs and sample selection. The distribution of PATH association probability (P_{host}) in the space of host-normalized offsets and AB magnitudes of 30 FRBs included in our sample is shown in panel a. We use the deepest available r-band or J-band imaging data for PATH analysis and compute the magnitudes and offsets, along with their measurement errors, using published catalogues or custom software (see Methods). We identified one case in which P_{host} is low because of high host-normalized offsets (dashed brown circle) and three cases in which P_{host} is low because of numerous plausible host galaxies (dashed

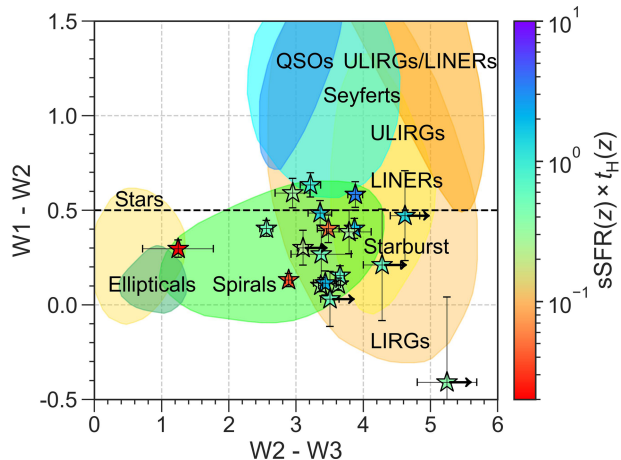
grey circles). Panel b shows the distribution of the r-band magnitude and redshift of 26 secure FRB hosts published in this work (squares), alongside Gordon et al.⁴ (circles) and Bhardwaj et al.⁵ (diamonds) FRB host galaxies samples with r-band magnitude $\lesssim 23.5$ (see Fig. 3 for a zoom-in on the $z \leq 0.2$ regime) and Type II CCSNe sample from ref. 37. For completeness, we also show the 5σ r-band limiting magnitude and the extragalactic DM of 12 DSA-110 hostless FRBs excluded from this sample (stars) and four insecure host associations (stars with cyan circles).



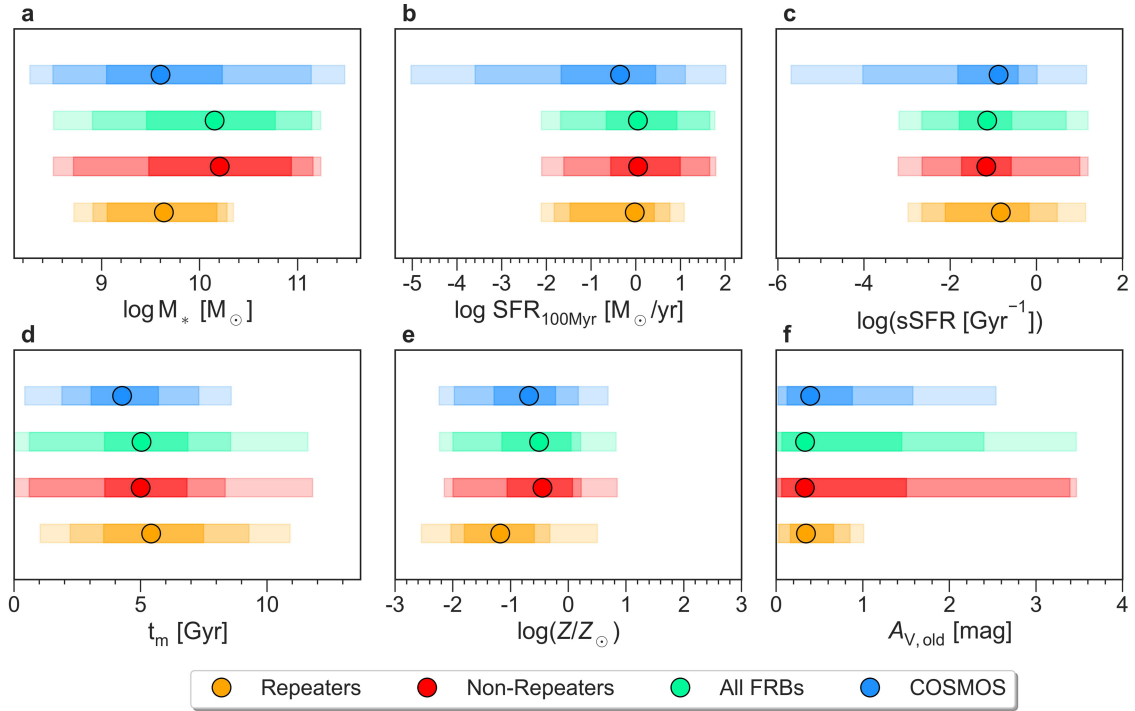
Extended Data Fig. 2 | Dominant ionization mechanism in FRB host galaxies.

The BPT empirical optical emission-line diagnostic diagrams using the optical line ratios $[\text{OII}]/\text{H}\alpha$, $[\text{SII}]/\text{H}\alpha$, $[\text{NII}]/\text{H}\alpha$ and $[\text{OIII}]/\text{H}\beta$ (ref. 30). The maximum starburst line¹²³, the pure star-forming galaxies versus Seyfert-H II composite objects classification line¹²⁴ and the Seyfert versus LINER classification lines³¹ are shown as solid, dashed and dotted lines, respectively. The emission-line diagnostics for SDSS galaxies are plotted in the background²⁶ (see Methods).

Although most of the FRB hosts spectra had the data to measure all of the emission-line ratios (green stars), some of them had limited spectral coverage, either because of a high redshift or because of instrument malfunctions. For these, we used the Prospector-derived SEDs to measure the line ratios (cyan circles). The error bars on green stars represent the measurement errors caused by noise in the spectrum and those on cyan circles represent the errors computed using 1,000 Prospector-derived posteriors of the galaxy SED.

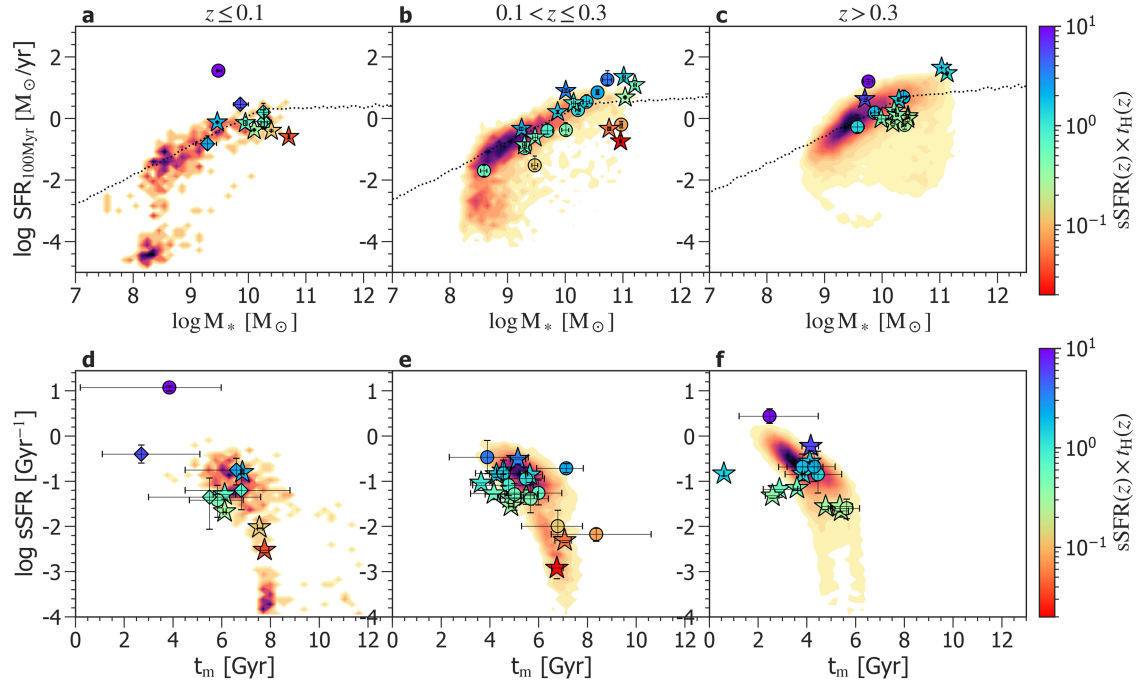


Extended Data Fig. 3 | WISE colour–colour galaxy classifications. This figure is adapted from ref. 32. The mid-infrared colours are retrieved using the publicly available WISE catalogue³². The shaded regions represent the standard WISE colour–colour classification regimes³². The dashed line marks the typical $W_1 - W_2 = 0.5$ boundary used to identify AGN activity in galaxies. The markers are coloured by the degree of star formation in FRB host galaxies¹²⁸.



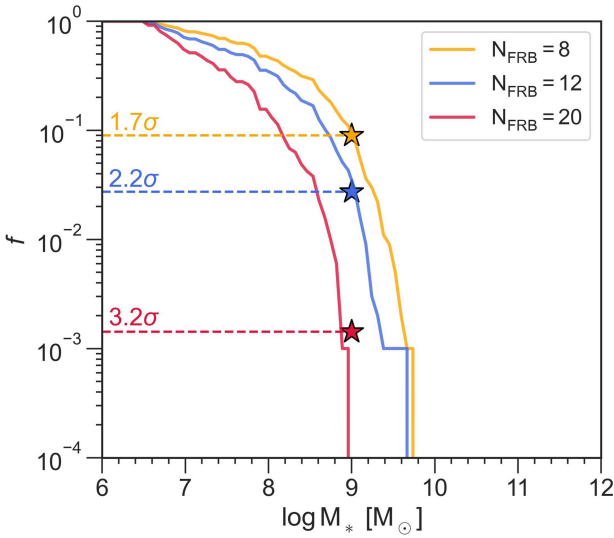
Extended Data Fig. 4 | Distribution of derived galaxy properties. We compare repeaters (orange), non-repeaters (red), all FRBs (green) and the background galaxy population (blue) from the COSMOS-2015 (refs. 33,92) and 3D-HST⁹³ galaxy catalogues. The FRB population includes our secure host associations and previously published FRBs^{4,5}. The marker denotes the median, together

with 1σ , 2σ and 3σ bands. We observe that the host galaxies of non-repeaters are relatively more massive, have lower sSFR and higher metallicity (potentially a consequence of enforcing the mass–metallicity relation in the SED modelling) than repeaters. However, KS tests reveal that these differences are not statistically significant (see Methods).

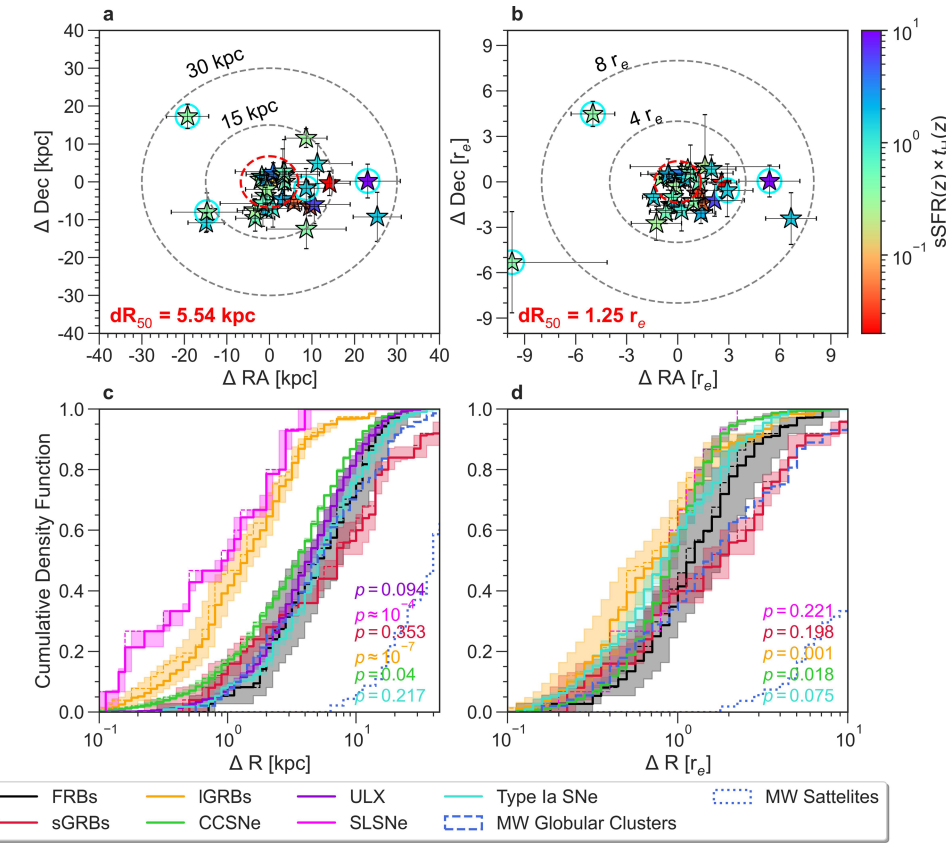


Extended Data Fig. 5 | Comparison of FRB host galaxies with background galaxy population. We use the COSMOS-2015 (refs. 33,92) and 3D-HST⁹³ galaxy catalogues to represent the field galaxy population. Along with the FRB host galaxies published in this work (stars), we also include samples from Gordon et al.⁴ (circles) and Bhardwaj et al.⁵ (diamonds). The insecure hosts are marked with cyan circles. The markers are coloured by the degree of star formation¹²⁸. The error bars are computed using 1,000 samples from the posterior distributions of measured properties from SED analysis. Panels a–c show the comparison with the SFMS of galaxies in three redshift bins to avoid

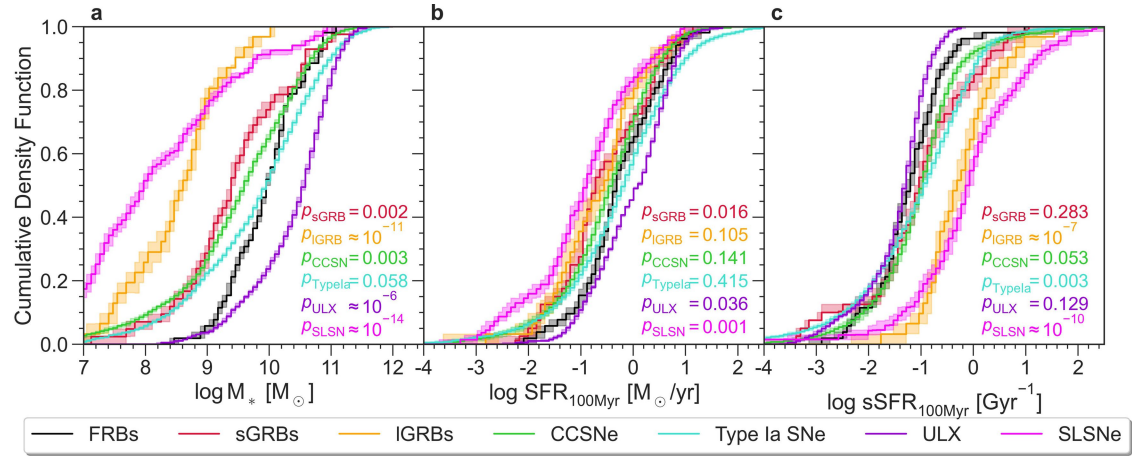
biases from redshift evolution. For reference, the centres of the SFMS at $z = 0.05, 0.20$ and 0.45 are marked as dotted lines³⁴. Although we observe a handful of quiescent galaxies, the distribution of the offset of each FRB host from the SFMS at their redshift³⁴ is centred at about -0.1 dex with a scatter of 0.7 dex, which is comparable with the intrinsic scatter of star-forming galaxies about the SFMS, implying that the FRB hosts are consistent with the locus of star-forming galaxies. This similarity with the background population is also seen in the comparison of ages and specific SFR in panels d–f.



Extended Data Fig. 6 | The importance of the lack of low-mass galaxies in FRB hosts sample. We draw 1,000 samples of size N_{FRB} of CCSNe host galaxies, in which N_{FRB} can be the number of FRBs localized by the DSA-110 (8, orange), localized by other instruments (12, blue) or all FRBs (20, crimson) at redshifts $z \leq 0.2$. For each stellar mass M_* , we plot the fraction of these 1,000 samples with no host galaxy more massive than M_* . Given the sample size of FRB host galaxies, we find that the CCSNe host galaxies above $10^9 M_\odot$ are rare with 3.2σ confidence.



superluminous supernovae (SLSNe)¹¹³, long-duration GRBs (IGRBs)¹¹⁵, core-collapse supernovae (CCSNe)^{37,112}, short-duration GRBs (sGRBs)¹¹⁹, Type Ia supernovae (SNe)¹¹⁷ and ultraluminous X-ray sources (ULX)¹²⁰. The measured values (dashed lines), medians (thick lines) and 1σ errors (shaded regions) computed using 1,000 Monte Carlo samples of offset measurements are plotted. We also show the galactocentric offsets of satellites¹³² and globular clusters¹³³ of the Milky Way (MW). Radio selection effects may prohibit the discovery of FRBs near the centre of the galaxies owing to high DMs and scattering timescales. If FRBs were to trace star formation, then this bias would overestimate the median of the distribution by around the order of a kpc (ref. 43).



To compare our FRBs with secure host association, together with previously published FRBs^{4,5}, against Type Ia supernovae (SNe)¹³⁴, ultraluminous X-ray sources (ULX)¹²⁰, superluminous supernovae (SLSNe)³⁷, core-collapse supernovae (CCSNe)³⁷, short-duration GRBs (sGRBs)¹¹⁸ and long-duration GRBs (IGRBs)^{39,114}, we correct for redshift evolution (see Methods). The errors on cumulative distributions are computed using 1,000 Monte Carlo samples of each measured property of the transients assuming a normal distribution with asymmetric errors.